

HOLE TRANSPORT LAYER OPTIMIZATION FOR METHYLAMMONIUM LEAD  
IODIDE PHOTOVOLTAIC CELL

by

Nischal Khakurel, B.S.

A thesis submitted to the Graduate Council of  
Texas State University in partial fulfillment  
of the requirements for the degree of  
Master of Science  
with a Major in Physics  
August 2020

Committee Members:

Alexander Zakhidov, Chair

Edwin Piner

Wilhelmus J Geerts

**COPYRIGHT**

by

Nischal Khakurel

2020

## **FAIR USE AND AUTHOR'S PERMISSION STATEMENT**

### **Fair Use**

This work is protected by the Copyright Laws of the United States (Public Law 94-553, section 107). Consistent with fair use as defined in the Copyright Laws, brief quotations from this material are allowed with proper acknowledgement. Use of this material for financial gain without the author's express written permission is not allowed.

### **Duplication Permission**

As the copyright holder of this work I, Nischal Khakurel, authorize duplication of this work, in whole or in part, for educational or scholarly purposes only.

## ACKNOWLEDGEMENTS

The completion of this thesis would not have been possible without the help from the following people I want to give my thanks to:

My research advisor Dr. Alex Zakhidov, for his constant support and guidance during the last two years. During my degree program, he has mentored me on a daily basis from which I have learnt a lot and have been able to shape myself to become a better scholar. His advice and encouragement will be very important in my future career development.

I would also like to thank my committee members Dr. Edwin Piner and Dr. Wilhelmus J. Geerts for putting their time and effort to offer insights into my work. Moreover, I would like to thank Dr. Craig Swartz who guided me to use the low temperature probe station and aided me during data collection, analysis and report preparation. He has not only helped with the probe station but has also constantly offered his insights and have reviewed my writing since day one.

I would like to thank Dr. Casey Smith and the entire staff of Analysis Research Service Center (ARSC) at Texas State University for providing trainings on the various characterization equipment. Additional personal thanks to Dr. Mehedhi Hasan and Kevin Lyon who trained me in the organic semiconductor lab during my starting days. Lastly, I would like to thank my group members: Garrett Merrion, Tanjina Ahmed, Mohammed Hossain, Drew Amyx, Leo Rodriguez, Rose Najar and Samuel Cantrell.

## TABLE OF CONTENTS

	<b>Page</b>
ACKNOWLEDGEMENTS.....	iv
LIST OF TABLES.....	vii
LIST OF FIGURES.....	viii
LIST OF ABBREVIATIONS.....	xi
ABSTRACT.....	xiii
CHAPTER	
1. INTRODUCTION.....	1
1.1 Background and Motivation.....	1
1.2 History of Perovskite and its properties.....	2
1.3 Perovskites in solar cells: optoelectronic properties and anatomy.....	4
1.4 Working Mechanism of a Solar cell.....	9
2. METHODS.....	19
2.1 Device Fabrication.....	19
2.2 Surface Profilometry.....	22
2.3 Atomic Force Microscopy.....	24
2.4 Ultra-Violet visible spectroscopy.....	25
2.5 Current-Voltage (J-V) Measurements.....	26
2.6 External Quantum Efficiency Measurements.....	26
2.7 Temperature and Light Intensity dependent measurements.....	28
2.8 Energy dispersive X-Ray Spectroscopy.....	28
3. RESULTS.....	29
3.1 Surface profilometry of Hole Transport Layer.....	29
3.2 Atomic Force Microscopy of Hole Transport Layer.....	31
3.3 Ultra-Violet Visible Spectroscopy of Hole Transport Layer.....	33
3.4 Current-Voltage (J-V) Measurements.....	35
3.5 Temperature and Illumination dependent measurements.....	48

3.6 Ion Migration in Hybrid Halide Perovskites.....	53
3.7 Energy dispersive X-Ray spectroscopy .....	60
4. CONCLUSIONS .....	65
APPENDIX SECTION.....	69
REFERENCES .....	72

## LIST OF TABLES

<b>Table</b>	<b>Page</b>
1. Recombination coefficients in MAPI .....	13
2. Performance metric averages for solar cell samples with PTAA HTL of different concentration.....	40
3. Two-Diode model fit parameters for champion device of 1.5mg/ml concentration of PTAA.....	44
4. Two-Diode model fit parameters for champion device of 2mg/ml concentration of PTAA.....	45
5. Two-Diode model fir parameters for perovskite solar cell with various PTAA HTL concentrations .....	46
6. Two-Diode model fit parameters for champion device of 3mg/ml concentration of PTAA.....	47
7. Two-Diode model fit parameters for champion device of 4mg/ml concentration of PTAA.....	48

## LIST OF FIGURES

<b>Figure</b>	<b>Page</b>
1. NREL Efficiency Chart .....	2
2. Crystal structure of Perovskite .....	3
3. Absorption spectra of various Hybrid Perovskites.....	5
4. Optical absorption of Si, GaAs and Hybrid Perovskite.....	6
5. Perovskite solar cell device structure (a) conventional and (b) inverted .....	7
6. Working mechanism of solar cell.....	9
7. Recombination mechanism in solar cell.....	13
8. Circuit model of a solar cell according to two-diode model .....	15
9. J-V Characteristic of a solar cell .....	15
10. S-Q limit curve.....	17
11. Patterned ITO anode (blue) to fit 4 devices .....	19
12. (a) Device architecture of solar cell with PTAA as a HTL (b) Energy band diagram of the solar cell.....	20
13. (a) Trench on the glass/ITO/PTAA sample scanned with a stylus probe (b) Step measurement using computer software.....	23
14. Block diagram of AFM.....	24
15. Block diagram of UV-Vis setup .....	26
16. Schematic diagram of EQE measurement setup.....	27
17. Profilometer results with average thickness for PTAA samples of different thickness.....	30

18. AFM images of PTAA HTL with precursor solution concentrations (a) 2, (b) 3 and (c) 4 mg/ml .....	32
19. Bar graphs of (a) root mean square roughness, and (b) vertical displacement of PTAA in toluene .....	33
20. UV-Vis transmittance spectra for PTAA on glass/ITO .....	34
21. Absorbance spectra for PTAA on glass/ITO with an inset of absorbance spectra to calculate bandgap.....	35
22. J-V curve for champion device with 2mg/ml concentration of PTAA HTL .....	37
23. External Quantum Efficiency of perovskite solar cell with 2mg/ml concentration of PTAA HTL .....	37
24. Statistical variation of performance metric for devices with different process parameters (a) PCE, (b) $V_{oc}$ , (c) $J_{sc}$ , (d) FF.....	39
25. J-V curve for champion device with 1.5 mg/ml concentration of PTAA .....	44
26. J-V curve for champion device with 2 mg/ml concentration of PTAA .....	45
27. J-V curve for champion device with 3 mg/ml concentration of PTAA .....	47
28. J-V curve for champion device with 4 mg/ml concentration of PTAA .....	48
29. The dark and illumination J-V characteristic of the PTAA HTL based perovskite solar cell with an inset of device parameters .....	50
30. Intensity-dependent characteristic of PTAA HTL based PV cell.....	52
31. Temperature-dependent Current-Voltage characteristic of perovskite solar cell .....	52
32. Light induced recovery of J-V curve for solar cells with PTAA HTL .....	55
33. Degradation and recovery of perovskite solar cells with PTAA HTL upon electrical bias .....	56
34. Capacitance transient after +1V pulse for devices with PTAA HTL .....	57

35. Interconversion of MAPI due to ion migration.....	58
36. Arrhenius plot of the decay rate of fast exponential component in a two exponential fit of capacitance decay for solar cell with PTAA HTL.....	59
37. Removal of Perovskite layer with triple DMF wash .....	61
38. EDX result for fresh device with PTAA HTL .....	62
39. EDX result of device without perovskite.....	63
40. Ion migration channels in hybrid halide perovskite.....	64
41. Standalone executable program for 2-diode fit.....	71

## LIST OF ABBREVIATIONS

<b>Abbreviation</b>	<b>Description</b>
PV	Photovoltaic
PCE	Power Conversion Efficiency
NREL	National Renewable Energy Lab
IBM	International Business Machines
HP	Hewlett Packard
LED	Light Emitting Diode
eV	electron Volts
Si	Silicon
GaAs	Gallium Arsenide
VBM	Valance Band Maximum
CBM	Conduction Band Maximum
DOS	Density of States
Pb	Lead
I	Iodine
TCO	Transparent Conductive Oxide
ITO	Indium Tin Oxide
Au	Gold
Al	Aluminum
Cu	Copper

ETM	Electron Transport Material
ETL	Electron Transport Layer
meV	milli electron Volts
HTM	Hole Transport Material
HTL	Hole Transport Layer
MAPI	Methyl Ammonium Lead Iodide
S-Q	Shockley-Queisser
PTAA	Poly[bis(4-phenyl)(2,4,6-trimethylphenyl)amine]
BCP	Bathocuproine
AFM	Atomic Force Microscopy
PZT	Piezoelectric scanner
EQE	External Quantum Efficiency
EDS	Energy dispersive X-Ray spectroscopy
FF	Fill Factor

## ABSTRACT

The innovation of hybrid halide perovskite solar cells has gained a noticeable advancement in the domain of photovoltaics. Despite of this upsurge in performance and its low cost, the materials that constitute a solar cell have different stability issues which hinder its performance and its commercialization. The hole transport layer is considered one of the most important material in perovskite solar cells. It plays a role in performance optimization, reducing recombination of charge carriers and aligning energy level with the contact layers. Besides hole transport layer, the perovskite methylammonium lead iodide itself is known be unstable at different temperatures, and, as a result, the device suffers from degradation. Temperature stability has also been associated with the phase change of the perovskite crystal structure. Moreover, the ions that constitute the perovskite layer are also known to be mobile which can have positive or negative effects to device performance. This work will investigate an organic polymer Poly[bis(4-phenyl)(2,4,6-trimethylphenyl)amine as a hole transport layer in methylammonium lead iodide perovskite solar cell. The devices made with this hole transport layer should enhance the device performance and even maintain its easy fabrication methods. The hole transport layer was first characterized for its physical and electrical properties after which the performance of the photovoltaic device was measured under standard AM1.5G solar illumination. The performance parameters were obtained by fitting the current-voltage curve employing a two-diode model. Device performance was also tested at different temperatures, which showed the phase transition of perovskite from orthorhombic to

tetragonal to cubic in the temperature range less than 165 K to 165 K to 327 K to temperature greater than 327 K respectively. Stability tests with light soaking and electrical biasing revealed that the degradation in device performance is indeed reversible due to ion-migration.

# 1. INTRODUCTION

## 1.1 Background and Motivation

Solar power is an important source of energy which can be utilized in producing electricity, heating, and cooling effects when desired. The energy radiating from the sun can be harnessed using different methods. More importantly, the energy we receive from the sun is renewable. We have been using fuels, coal, gas and oil, to create energy; all of which are non-renewable. The sun produces electromagnetic radiation which can be directly utilized to produce electricity. This process is known as Photovoltaic (PV) effect. When the right semiconducting materials are incorporated together to form a working device, this device produces electric current when exposed to the light (electromagnetic radiation) from the sun. The electrical energy can be used to power electrical equipment and also to recharge a cell.

The PV effect was discovered by the French Scientist Edmond Becquerel in 1839[1] in his father's laboratory when experimenting with coating silver chloride on platinum electrodes. Current and Voltage were generated when the electrodes were illuminated with light. The first solar cell was created by a New York scientist Charles Fritts. The invention was possible by coating selenium with a thin layer of gold. However, the power conversion efficiency (PCE) of this solar cell was only 2%.[2] The efficiency of the solar cell made it impossible for practical uses. In 1954, scientists Gerald L. Pearson, Daryl M. Chapin and Calvin S. Fuller at Bell Laboratories replaced the use of selenium with silicon and made the first solar cell that had a PCE of 6%.[3] This led to the start in research and advancement of solar cells and their application in spacecrafts, household, military and commercial areas.

National Renewable Energy Laboratory (NREL) has been maintaining a chart[4] since 1974 which shows the progress in PCE of different solar cell technologies. The chart in Figure 1 shows that there is a slow increase in efficiency among various modules. But we can see that there is an exception among the modules: Perovskite Solar cells. There is a sharp rise in PCE for Perovskite Solar cells, which is of much interest and the center of this work.

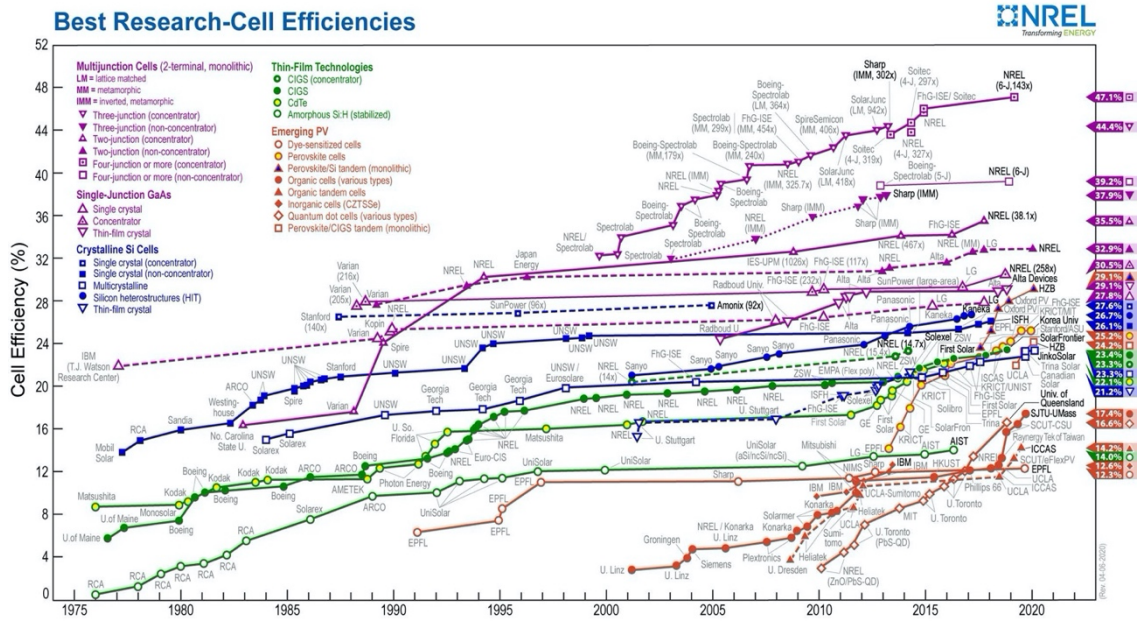
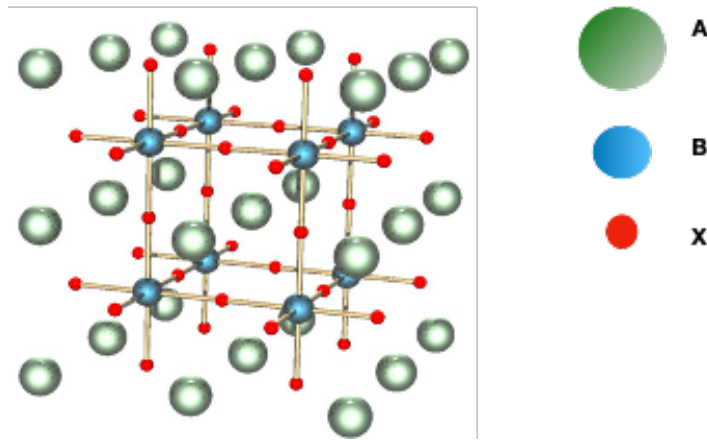


Figure 1: NREL Efficiency Chart [4]

## 1.2 History of Perovskite and its properties

Perovskite is a class of materials which was first discovered in 1839 at the Ural Mountains in Russia by Gustav Rose and Lev Perovski. The mineral which was discovered consists of calcium titanate ( $\text{CaTiO}_3$ ) whose structure is now known as perovskite structure. Any crystalline material whose cubic unit cell consists of  $\text{ABX}_3$ , where A and B are cation type molecules and X represents anion type molecules[5] is

known as a Perovskite. The structure of perovskite is shown in Figure 2. In the figure, the red sphere denotes X atoms, blue the B atoms and green spheres are A atoms. Perovskites have been extensively studied since the 1940s because of their various physical properties such as superconductivity, magnetoresistance, ferromagnetism, piezoelectric effect, thermo electric effect, and of major importance in this work, their photovoltaic properties.



**Figure 2: Crystal structure of Perovskite [5]**

There is a unitless constant associated with the crystal structure of a perovskite, namely the Goldschmidt relationship. This relationship gives the information regarding the crystallographic stability of a perovskite structure. The relationship is given by a tolerance factor ‘t’:

$$t = \frac{R_A + R_X}{\sqrt{2(R_B + R_X)}} \quad (1)$$

Where,  $R_A$ ,  $R_B$  and  $R_X$  are the radii of ionic molecules A, B and X respectively. For an ideal perovskite the value of tolerance factor is 1. But, in practice a stable hybrid

perovskite (HP) structure has a tolerance factor of  $0.89 < t < 1$ . [6]

Hybrid Halide Perovskite was firstly synthesized by Dieter Weber. He was able to successfully describe the crystal structure but lacked to describe its electronic property. He concluded in his work that the material was insulating. [7] It was in 1999 that a more overall modern comprehensive study was done by David Mitzi of IBM. He made a lot of material science progress but, was not able to realize the potential photovoltaic application of HP. [8] The first use of hybrid halide perovskite for photovoltaics was done by *Kojima et al.* in 2009 [9]. Methylammonium lead bromide ( $\text{CH}_3\text{NH}_3\text{PbBr}_3$ ) and Methylammonium Lead Iodide ( $\text{CH}_3\text{NH}_3\text{PbI}_3$ ) were used to construct a working photovoltaic cell. They yielded a PCE of 3.13% and 3.81% respectively. Then, perovskite quantum dot synthesized solar cells were made by *Park et al.* which had a PCE of 6.5%. [10] Since then, the same concept has been improved and further utilized to produce PV cell using hybrid halide perovskite which has reached a maximum PCE of 23.7% in the present day. [4] Now that a brief history of perovskite has been discussed, the properties of hybrid halide perovskites and its anatomy in PV cells will be explained in the next section.

### **1.3 Perovskite in solar cells: optoelectronic properties and anatomy**

In the structure of perovskite, the cation 'A' is located at the center. The organic cation can be either methylammonium (MA), formamidinium (FA) and phenylammonium (PhA). The metal cation 'B' can be Lead (Pb) or Tin (Sn) and the halide anions 'X' can be Chlorine 'Cl', Iodine 'I' or Bromine 'Br'. [11] These molecules when combined together can absorb from visible to near infrared range (350 – 950

nm).[12] The change in cation or the changing or mixing of the halide ion causes the onset of the absorption to change. This is depicted in Figure 3[13]. This onset in absorption means that by changing or mixing the molecules, the bandgap of a perovskite can be tuned. Studies have shown that the bandgap of perovskite can be tuned within a range of 1.3 eV to 2.3 eV.[14]

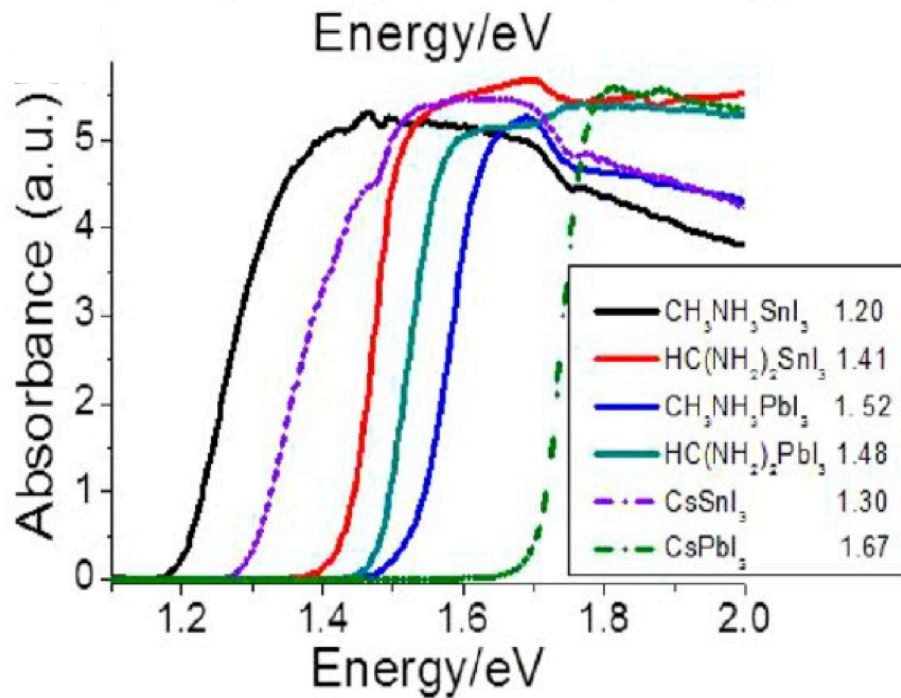


**Figure 3: Absorption spectra of various Hybrid Perovskite [13]**

Hybrid halide perovskites have been mostly used in optoelectronic devices such as photovoltaic cells and light emitting diodes (LED). In this work, methylammonium lead iodide ( $\text{CH}_3\text{NH}_3\text{PbI}_3$ ) will be used for its PV properties. We use  $\text{CH}_3\text{NH}_3\text{PbI}_3$  because the bandgap of the material is 1.52 eV [13]. This is close to the energy required to maximize the power absorption of the solar spectrum, i.e at 1.34 eV.[15] Moreover, perovskite absorber layer which is less than 500nm thick, can absorb enough sunlight to achieve a

PCE of about 15%. A layer this thin means that the device can be lightweight, has low fabrication costs and can be potentially flexible. Hybrid perovskites have optical absorption close and even better than first- and second-generation absorbers such as Silicon (Si) and Gallium Arsenide (GaAs). Perovskite and GaAs are direct bandgap materials and Hybrid Perovskites have superior optical absorption to that of Si and GaAs because their Valance Band Maximum (VBM) and Conduction Band Minimum (CBM) are formed from mixing of Pb s, I p and Pb b orbitals respectively. This fact enables the Density Of State (DOS) to be high, as the p-orbital is degenerate having six states,  $m = -1, 0$  and  $1$ . Each of these states have a factor of two associated with the spin making a total of six states in the p-orbital.[16] This fact elucidates that perovskites have high optical absorption.

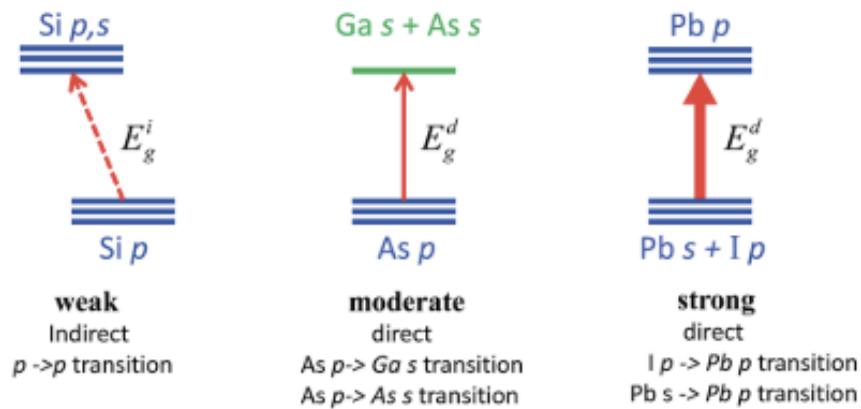


**Figure 4: Optical absorption of Si, GaAs and Hybrid Perovskite [16]**

To incorporate this perovskite in an organic perovskite solar cell, there are two architectures, namely: (a) planar n-i-p, or conventional, and (b) planar p-i-n, or inverted, solar cell. The schematics of both architecture are shown in Figure 5a and 5b

respectively.[17] The solar cells produced for this work will have inverted structure.

For a proper functionality of a solar cell, the sunlight should be able to reach the perovskite layer. Hence, the cathode or anode for conventional or planar structure should

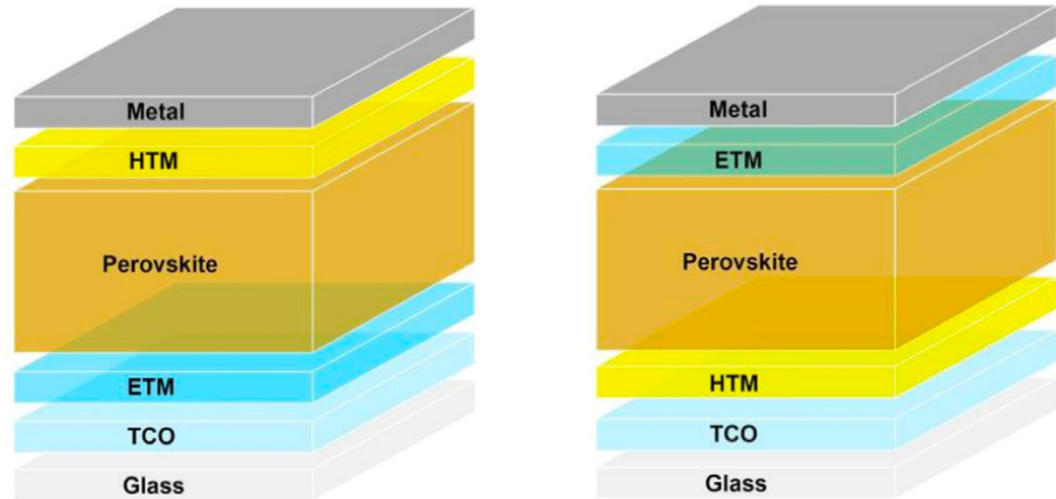


**Figure 5: Perovskite solar cell device structure (a) conventional and (b) inverted [17]**

be transparent to the incoming radiation. This requirement enforces that the electrode on glass should be able to transmit the light within wavelength range from 400nm to 800nm. So, a transparent conductive oxide (TCO) such as indium tin oxide (ITO) is required. For electrical contact the back-side electrode can be any metal, gold (Au), aluminum (Al), or copper (Cu). Now, the radiation passes through hole transport material (HTM) or hole transport layer (HTL), which is spin coated on top of the TCO. By the name, this layer must effectively transmit the incoming light and should have high hole mobility and a very high conduction band offset so that it does not allow the electrons to pass through.[18][19]

As the light is now absorbed by the perovskite layer, the layer above it, the electron transport material (ETM) or electron transport layer (ETL) does not need to be

transparent. In difference to the HTL, the ETL should have high electron mobility, a high electron concentration large valance band offset to block the holes and to effectively allow transmission of electrons. [18][19] In other PV technologies, such as Silicon, p-type or n-type doping is done in order to create a built-in electric field. This would be an easy way to extract charge carriers out of the intrinsic layer and achieve high efficiency, as a p-n junction has higher PCE limit than a p-i-n structure.[20] However, this cannot be realized in Perovskite PV as no reliable doping strategy for Hybrid perovskite solar cells has yet been implemented. There have been certain attempts[21][22] to do so, one of them is by ion implantation. But this process requires high temperature treatment which hybrid perovskites cannot withstand. Hence, the use of a HTL and ETL is necessary in perovskite solar cells to extract the carriers from the Hybrid perovskite layer.

The perovskite layer is spin coated on top of the HTL. The perovskite layer has a polycrystalline morphology. Further details on the spin coating processes of the HTL, perovskite films and thermal evaporation of ETL, and the materials used for this work will be discussed in the device fabrication section. Also, the functionality of a solar cell with an appropriate model with the performance parameters will be explained in the next section.

## 1.4 Working Mechanism of a Solar cell

This section will focus on the working principle of solar cell when perovskite is incorporated with other layers to make a full device. A device that is capable of converting the light energy to electricity by photovoltaic effect is known as a solar cell. Generally, it is a semiconductor device also synonymously called a photodiode. After the generation of electron-hole pair in the intrinsic layer, they are collected by the front and back contacts. The current produced during this process is called *photogenerated current*. Moreover, the p layer and n layer are heavily doped with respective charge carriers which create a high electric field in the intrinsic layer, in our case, the perovskite which is fully depleted. The basic operation of a solar cell is shown in Figure 6.

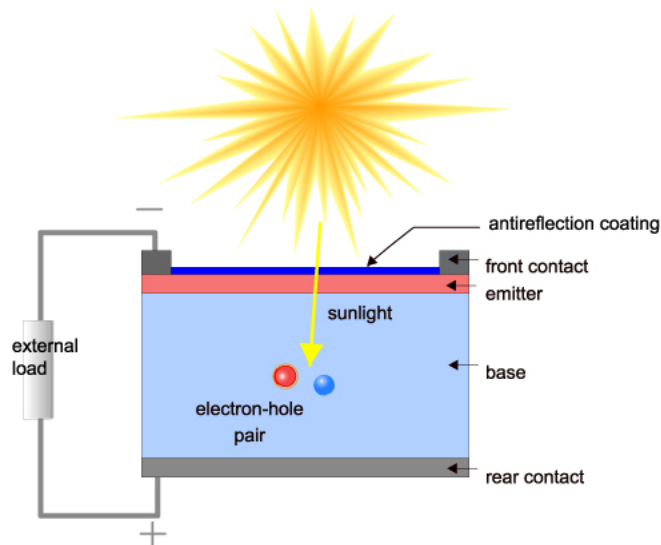


**Figure 6: Working mechanism of a solar cell [23]**

The role of excitons is often scrutinized in various Hybrid Perovskites. They are bound electron hole pairs which are created when a photon interacts with the crystal. They are electrically neutral, and their transport mechanism is based on diffusion rather than drift. Moreover, at room temperature under 1-sun illumination intensity there are

very few numbers of excitons and the exciton binding energy is only 10meV which is much smaller than the thermal energy 25meV. This fact elucidates that they should quickly dissociate at room temperature. So, despite of having some effects on the absorption onset, they are not considered as major carriers.[24]

When a photon is incident on a material and gets absorbed, the electrons get excited from the lower energy state and gets transferred to higher energy state. According to quantization of energy[25], the energy levels inside a material are quantized. The energy of the incident photon is given by the relationship:

$$E = \frac{hc}{\lambda} \quad (2)$$

where  $c$  is the speed of light,  $h$  is Planck's constant and  $\lambda$  the wavelength of incident light in vacuum. Moreover, if the energy of the photon is insufficient to excite the electron, the photon is transmitted rather than absorbed by the material. The energy difference between the lower (valance band,  $E_v$ ) and higher energy level (conduction band,  $E_g$ ) is known as a band gap,  $E_g$ . This imposes a requirement that the incident photon must have an energy sufficient enough to transfer the excited electron to the higher states. The generated electron-hole pair is bound together by a coulombic force as they have opposite charge. The process of recombination involves the electron going back to a lower energy state which it left before in the valance band.

There are mainly three basic types of recombination in a bulk semiconductor. They must be minimized in a solar cell as they cause a loss in current. In the case of radiative recombination, this process also causes the emission of a photon which has the energy corresponding to the band gap. This might be reduced through applying a bias voltage which separates the carriers. The radiative recombination process is also considered the

most prevailing mechanism of recombination in direct bandgap semiconductors. However, in the case of perovskite solar cells, some studies have shown that the mechanism of radiative recombination is not a dominating recombination mechanism.[26][27] The mechanisms are shown in Figure 7. In contrast to these studies it has been reported that the ionic materials that constitute a hybrid halide perovskite can self-trap to form polarons. Large polarons are described to be quasiparticles that spread through the lattice and cause lattice distortion. This spreading of the polaron is thought to be the reason of suppressed band to band recombination in hybrid halide perovskites. [28] Due to the spin orbit coupling in hybrid halide perovskites, the splitting of bandgap at k-point also causes the material to transition into an indirect bandgap material which slows down the recombination process.[29] Photon recycling is also a prevalent mechanism in hybrid perovskites, in which, the band-to-band recombination results in an emission of photon which is again absorbed by the perovskite. This emission of photon also does not experience any electrical resistivity losses.[30] Besides photon recycling, band-to-band recombination in perovskites is also believed to be suppressed due to the spontaneous polarization resulting in ferroelectric domain that separates the excited electron and hole pairs which, as a result, suppresses the band-to-band recombination.[31]

There are also some other mechanisms of recombination that arise due to crystal defects. These defects give rise to what is called a trap state inside a material's band gap. In the case of hybrid perovskites, defects or impurities are located in grain boundaries and at the surface of the film.[32][33][34] Moreover, the perovskite layer is usually sandwiched between an ETL and HTL. Besides the defect in crystal structure, some defects are present at the surface and the interface between the semiconductor. Discrete

energy levels are formed due to defects within the bulk and due to impurities. As the perovskite layer is grown by spin coating a solution, it is quite obvious for the layer to have visible defects such as pinholes or non-uniform coverage, but these can be mitigated by optimizing the growth parameters. However, defects such as interstitials, vacancies and point defects are not visible to bare eyes and are obviously present within the perovskite layer because of how it is processed. Yet *Yin et al.* [35] showed that the formation energy of the defects is relatively low (less than 0.05 eV below CBM) and defects responsible for creating deep traps have high formation energy (above 2 eV). This means the defects are not as bad compared to other disordered materials. Hence, the high formation energy for deep levels which is responsible for non-radiative recombination indicate that,  $\text{CH}_3\text{NH}_3\text{PbI}_3$  has less low non-radiative recombination. Also, the recombination mechanism can be attributed to the interface between transport layers which also act as recombination center for charges and some defects that gives rise to deep traps. Due to these states within the band gap, the electrons do not reach the valance band to recombine but reach the trap state at first and get transferred to the valance band later. This process is called Shockley-Read-Hall recombination. Aside from these photophysical process in hybrid halide perovskite, small polarons have also been studied to better understand the recombination mechanism. These quasiparticles are located on a few lattice sites and control the charge carrier transport whose accumulation is believed to cause various trapping sites within the band structure of MAPI.[36][37] Also the formation of small polaron happens in a large time scale which allows them to capture hole then electron then hole and so on.[37] Besides these two recombination mechanisms, there is one another mechanism that comprises three charge carriers. This mechanism is

known as Auger recombination. The Auger recombination process is non-radiative, i.e. the energy from the recombination is given out to a third carrier in the conduction band. This electron then traverses back down to the conduction band edge. Auger recombination is only mostly considered in Silicon based solar cells as this process is caused by high carrier concentration and doping, [38] which is not dominant in hybrid perovskites. The recombination coefficients reported on various literatures for methylammonium lead iodide is tabulated in Table 1. These coefficients are obtained using different carrier injection conditions. The mathematical quantity that describes the recombination process is known as the *ideality factor*. This parameter will be discussed in more detail while explaining the diode model for a solar cell.

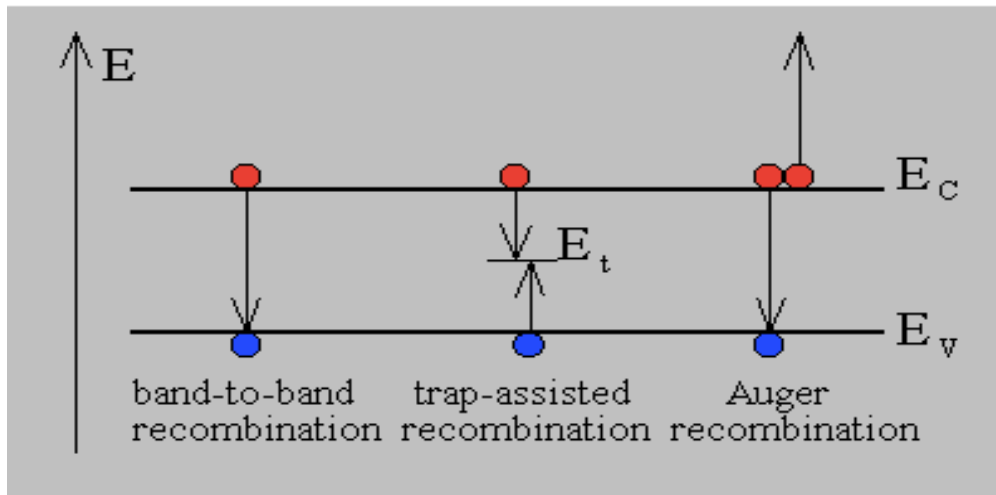


Figure 7: Recombination mechanism in a solar cell [38]

Table 1: Recombination coefficients in MAPI [39][40]

Mechanism	Diode Ideality Factor	Carrier Concentration	Rate	MAPI Values ( $\text{cm}^3/\text{s}$ )
Shockley-Read-Hall recombination	1 or 2	$n^2$	$n^2 \cdot k_2$	$0.6 \cdot 10^{-6} - 10^{-10}$
Band-to-band recombination	1	$n$	$n \cdot k_1$	$15 \cdot 10^{-6} - 10^{-10}$
Auger recombination	3	$n^3$	$n^3 \cdot k_3$	$10^{-10} - 1.6 \cdot 10^{-28}$

There are certain parameters that can be extracted from a solar cell. The most important parameter is known as its power conversion efficiency. This PV-process in solar cell can be modeled by a circuit using a diode, and a series and shunt resistance. The equivalent model is shown in Figure 8. the current through the solar cell is given by the equation:

$$J = J_{ph} - J_o \left[ \exp\left(\frac{qV}{nkT} - 1\right) - \frac{V + JR_s}{R_{sh}} \right] \quad (3)$$

where,  $J_{ph}$  is the photocurrent,  $J_o$  is the reverse saturation current,  $n$  is the ideality factor,  $R_s$  and  $R_{sh}$  are the series and shunt resistance respectively and  $V$  the voltage applied across the solar cell. However, this model accounts only one ideality factor for the recombination process occurring within the solar cell. Because of this we will be using a two-diode model which is shown in Figure 8. This model includes two ideality factors which will try to elucidate the two types of recombination mechanisms for the solar cell fabricated in this work. The current from the solar cell using this model is given by:

$$J = J_{ph} - \frac{V + JR_s}{R_p} - J_{o1} \left( e^{\frac{q(V + JR_s)}{n_1 kT}} - 1 \right) - J_{o2} \left( e^{\frac{q(V + JR_s)}{n_2 kT}} - 1 \right) \quad (4)$$

In this model, the current under illumination is given by  $J_{PH}$ . The two diodes  $D_1$  and  $D_2$  have corresponding current  $J_1$  and  $J_2$ . The diode  $D_1$  is used to model radiative recombination, hence the ideality factor for it,  $n_1$  is 1. The diode  $D_2$  will be used to model Shockley-Read-Hall recombination.  $R_s$  is the series resistance that will arise due to the different components in the device. The shunt resistance,  $R_p$ , occurs due to unwanted shorting in the device. It serves as a low resistance path for charge carriers to conduct that is parasitic to photocurrent.[41] The external current and voltage is given by  $V$  and  $J$  respectively.  $J_{o1}$  and  $J_{o2}$  are the saturation current through diode  $D_1$  and  $D_2$  respectively.

$\frac{kT}{q}$  is also known as the thermal voltage.

There are certain parameters that are of interest in a solar cell. The short-circuit current  $J_{SC}$  is the maximum current that can be obtained from a solar cell when the voltage across the device is zero. This parameter depends on the generation of photogenerated carriers. Another quantity of interest is the open circuit voltage that can

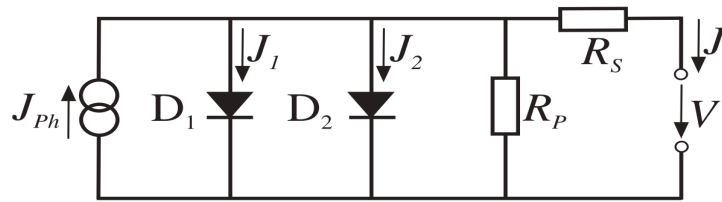


**Figure 8: Circuit model of a solar cell according to two-diode model [42]**

be obtained from a solar cell when the current is zero. For a single diode, it is given by the formula :

$$V_{oc} = \frac{nkT}{q} \ln \left( \frac{J_{ph}}{J_o} + 1 \right) \quad (5)$$

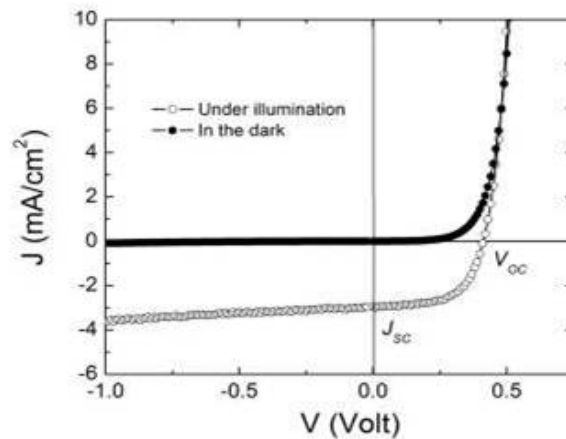


**Figure 9: J-V Characteristic of a solar cell [43]**

where  $\frac{kT}{q}$  is the thermal voltage. We can see that it is a temperature dependent term. The dependent of open circuit voltage on temperature will also be investigated in this work. A typical Current-Voltage (J-V) characteristic of a solar cell is shown in Figure 9. When a solar cell is illuminated, the curve shifts down and generates power. The greater the illumination, the greater is the power generated from the solar cell. The power generated at both open circuit condition and short circuit condition is zero, as  $P=VI$ . So, to extract maximum power from a solar cell, the current and voltage have to have a certain magnitude. The fill factor (FF) is another term which is defined as the ratio of maximum power from a solar cell to the product of open circuit voltage and short circuit current. The FF is also a measure of squareness of the J-V curve. Mathematically, it is given as:

$$FF = \frac{P_{max}}{J_{sc}V_{oc}} \quad (6)$$

Now, the most important parameter, the power conversion efficiency (PCE) is defined as a ratio of generated power over the total power of solar spectrum received on Earth,  $P_{sol}$  [44]. It is given by:

$$\eta = \frac{P_{max}}{P_{in}} = \frac{J_{sc}V_{oc}FF}{P_{sol}} \quad (7)$$

where, the magnitude of  $P_{sol}$  is  $100\text{mW}/\text{cm}^2$ . [44] This magnitude of power is used to simulate irradiance, which is the standard spectrum that reaches the earth's surface also known as AM 1.5G. [45]

The theoretical limit on maximum PCE[46] for a solar cell is known as Shockley-Queisser (S-Q) limit. This was calculated by Hans-Joachim Queisser and named in the honor of Schokley for his work in the development of diode model which was based on the generation, recombination, and carrier transport equations. The S-Q limit will be discussed in short with some physical considerations: absorption loss, black-body radiation loss and radiative combination loss to determine the highest PCE achievable in a solar cell. The maximum achievable PCE as a function of the bandgap is shown below:

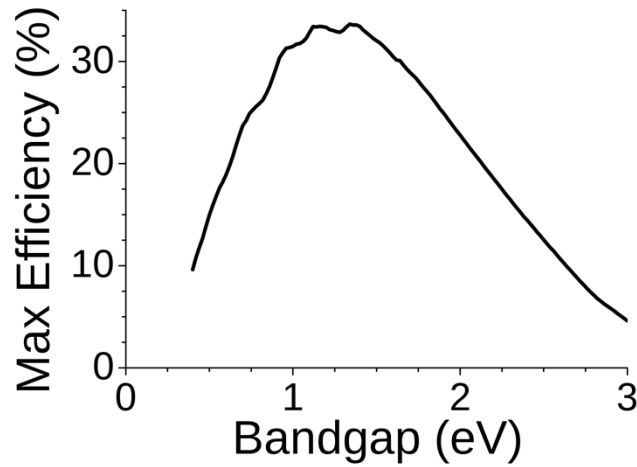


**Figure 10: S-Q limit curve [46]**

The S-Q limit for any solar cell has been calculated to be 33.7%.[46] The PCE is increasing with bandgap at low photon energy and decreases when the bandgap passes 1.34 eV. It is smaller in practical devices as the HTL starts absorbing the incoming light which, as a result, does not reach the perovskite layer. For hybrid perovskites, the limit is 30.1%.[47] But, till this date, the maximum reported efficiency is 25.2%.[4] So there is significant room for improvement. There are several ways to optimize the PCE, some of

them are tuning the bandgap by mixing halides in the perovskite layer, changing the ETL, use of a tandem structure, or use of another HTL. The main focus of this work is to optimize the HTL to increase the device's performance. The structure of the device used in this work and the properties of the HTL will be investigated in the device fabrication section.

## 2. METHODS

Now that we have explained the various principles and theory underlying the working principle and importance of a perovskite solar cell, this section will explain about device fabrication and the various characterization techniques used for device and HTL characterization. The HTL will be characterized using numerous techniques for thickness and its uniformity, roughness, and its band gap. Several other techniques such as External Quantum Efficiency measurement, Current Voltage (J-V) measurement, *etc.* will be employed for device characterization.

### 2.1 Device Fabrication

The devices produced in this research will have an inverted heterojunction architecture (p-i-n) using  $\text{CH}_3\text{NH}_3\text{PbI}_3$  (MAPI) as the intrinsic layer. The device architecture will be glass/ITO/PTAA/ $\text{CH}_3\text{NH}_3\text{PbI}_3$ / $\text{C}_{60}$ /BCP/Al. The patterned Indium Tin Oxide (ITO) layer comes pre-deposited on an 1 inch square silicate glass slide. The pattern is such which will allow 4 devices per slide. The pattern is shown in Figure 11. The device architecture with the appropriate band gap is shown in Figure 12.

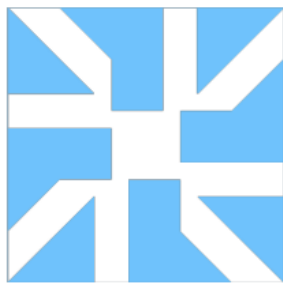


**Figure 11: Patterned ITO anode (blue) to fit 4 device**

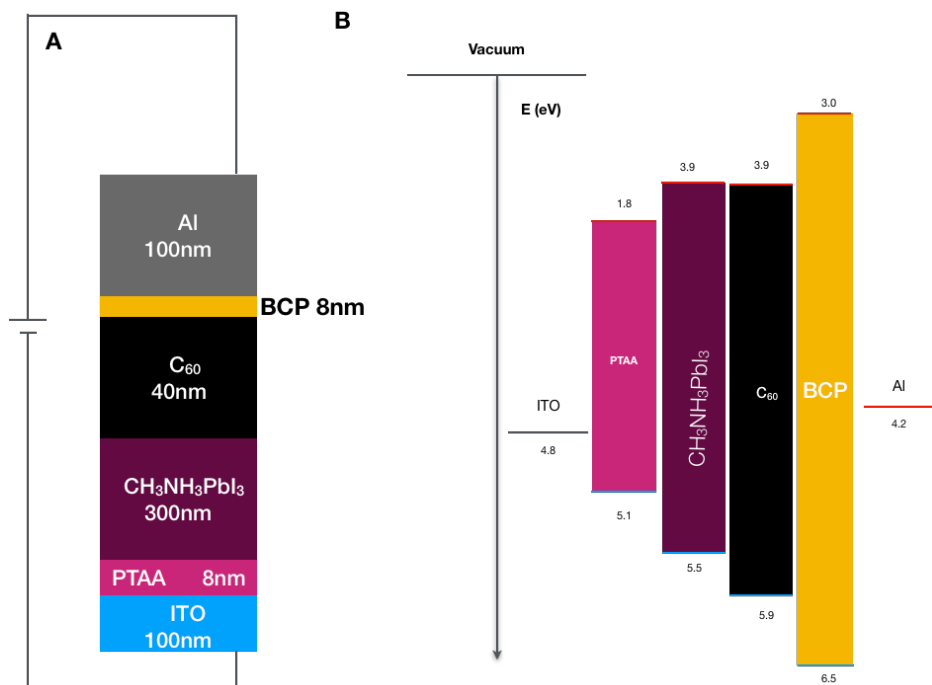


**Figure 12: (a) Device architecture of solar cell with PTAA as a HTL (b) Energy band diagram of the solar cell**

The device fabrication process starts with ultra sonicating glass/ITO slides in Deconex OP 121 detergent and deionized water. After ultra sonicating for 20 minutes in Deconex OP 121, the slides were rinsed with deionized water followed by ultrasonication for another 20 minutes. The cleaned substrates were then dried using a Carbon dioxide (CO<sub>2</sub>) gun. Then, a final plasma treatment was performed for 10 minutes to remove any sort of organic contamination remaining on the surface. The cleaned slides were brought inside the N<sub>2</sub> filled glovebox with ~0ppm Oxygen level (O<sub>2</sub>) and moisture.

To make a PTAA solution, commercially available PTAA powder was used. Solutions of various concentrations of PTAA ranging from 1.5 mg/ml to 4 mg/ml was made by dissolving the powder in toluene at room temperature. The underlying reason to make various concentration of PTAA solution was to compare the thickness and PCE of

the devices fabricated. All the solutions were spin coated on the glass/ITO slides using a consecutive step recipe. Two step recipe was used as it is the easier and preferable way to remove edge beads to improve spin coating uniformity.[48] To spin coat the solutions, 120  $\mu$ l was spin coated on the glass/ITO substrates. The first step of the spin coater was left constant at 500 rotations per minute (RPM) for 4 seconds and the second step was varied between 1500 rpm, 3000 rpm and 4500 rpm. The PTAA thin films were annealed at 110°C for 10 minutes to evaporate any remaining solvent in the slide.

The HTL optimization was done by making devices in batches by varying concentration and spin speeds, one at a time. The goal of this process was to produce the best quality HTL along with the best photovoltaic parameters. The HTL layers above 1500 rpm had fewer pin holes, which was clearly visible through naked eyes for higher concentrations. The maximum PCE obtained using 1.5 mg/ml, 2mg/ml, 3 mg/ml and 4 mg/ml concentration of PTAA were 16.6%, 17.7%, 16.4% and 15.27% respectively. Also, the concentration of 1.5mg/ml resulted in a very thin HTL (less than 8nm) which was doubted even to function as a HTL. This also was proven when the device parameters were far less than optimum.

The stability of the HTL was also studied by storing the devices in vacuum and inside the N<sub>2</sub> filled glovebox. Also, the stability of device under electrical stress and light soaking will be addressed later on.

The CH<sub>3</sub>NH<sub>3</sub>PbI<sub>3</sub> (MAPI) perovskite ink was prepared by mixing equal molar parts of lead iodide (PbI<sub>2</sub>), methylammonium acetate (CH<sub>3</sub>NH<sub>3</sub>CH<sub>3</sub>COOH), and methylammonium iodide (CH<sub>3</sub>NH<sub>3</sub>I) dissolved in dimethylformamide (DMF) at 1.0 M concentration. The solution was then deposited onto the glass/ITO/PTAA inside a dry N<sub>2</sub>

glovebox at 4000RPM for 60 seconds. Then the glass/ITO/PTAA/MAPI structure was annealed on a hotplate in atmosphere with 30%-40% humidity for 10 minutes to produce multicrystalline perovskite film. The devices annealed in this humidity produced better crystals of perovskite.[49] The structure was scraped using a mask to separate the devices. The dust from scraping was blown using a N<sub>2</sub> gun. After this process, the devices were brought inside the N<sub>2</sub> filled glovebox to deposit the ETL.

The remaining ETLs C<sub>60</sub> and bathocuprione (BCP) were deposited on the device area by thermal evaporation. The thickness of deposited C<sub>60</sub> and BCP was 40 nm and 8 nm respectively. There are studies which showed that the use of BCP reduced the undesirable band bending which with otherwise occur if the C<sub>60</sub> was in direct contact with the cathode.[50]

An aluminum (Al) cathode of 100nm was thermally evaporated with an appropriate pattern to act as the device cathode. The device was then taken out of the evaporator and encapsulated by using an encapsulating printer with glass caps to seal the devices. The final device was removed from the glovebox and painted with silver (Ag) ink to make contacts for further electrical characterization.

## **2.2 Surface Profilometry**

The thickness of HTL plays a crucial role in device optimization. If the HTL layer is too thin or too thick, there are issues such as pinholes or non-uniform coverage on the glass/ITO slides which result in low PCE.

Stylus profilometry is a technique in which a scanning probe is brought into contact with the surface of the sample to be scanned. The stylus is trailed on the sample to generate a thickness profile based on the spatial coordinates of the stylus. To measure the thickness, the sample needs to have a trench or a step which enables the stylus to generate a step height. This step height is used to measure the thickness of a film. To measure the thickness of the HTL, a trench was made on the glass/ITO/PTAA surface. It is evident that the trench causes damage to the sample. But, this is not of major concern as the samples comparatively require less thermal processing and are relatively inexpensive compared to other materials grown using molecular beam epitaxy (MBE) or e-beam evaporation. In this work, the Bruker DektakXT stylus profilometer was used. The radius of the tip is 2  $\mu\text{m}$  and a force of 3mg for the scans. The thickness profile, profilometer and trench on the sample are shown in Figure 13

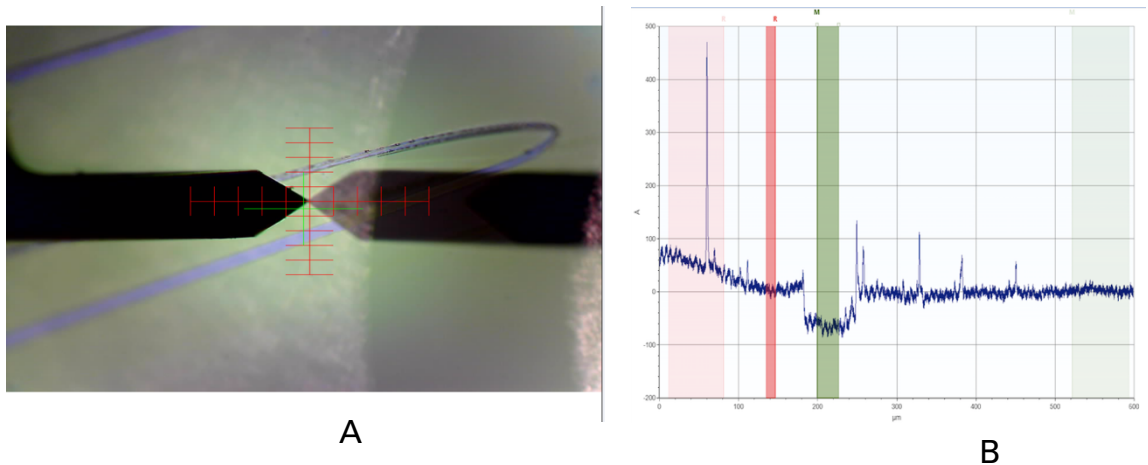


**Figure 13: (a) Trench on the glass/ITO/PTAA sample scanned with a stylus probe (b) Step measurement using computer software**

## 2.3 Atomic Force Microscopy

Atomic force microscopy (AFM) is a scanning probe technique (SPM) in which a mechanical probe is used to contact the sample surface to produce topographical images in 3D. The schematic diagram of an AFM setup is shown in Figure 14. The tip is located at the end of the cantilever which is attached to a piezoelectric (PZT) scanner. When a bias is applied to the scanner the tip scans over the sample surface. The tip is either deflected or bent due to the force of repulsion or attraction when the tip is near the sample surface. This deflection is detected by the photodiode through the laser reflected from the cantilever vibration. The signal through the photodiode is processed by a computer to produce topographical data. There are two scanning modes in an AFM: contact and tapping. The tapping mode is more commonly used as this method does not tamper with the sample's surface. In this work, basic tapping mode is used to measure roughness and image the surface morphology of PTAA HTL of various concentrations. The HTL films for this characterization were deposited on completely coated ITO.

A Bruker Dimension ICON Scanning probe microscope was used to study the roughness and topography of the samples.

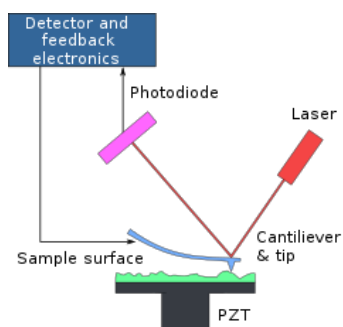


**Figure 14: Block diagram of AFM [51]**

## 2.4 Ultra-Violet visible spectroscopy

Ultraviolet – Visible Spectroscopy (UV-Vis) is a type of characterizing technique that is applicable in determining a material's band gap and chemical structure. As suggested by the name, it uses UV light, produced by a monochromator and a light source, which is passed through the sample and is detected by the photo detector on the other side. Based on the amount of light reaching the photo detector, the absorbance, reflectance and transmittance spectrum is produced. A schematic diagram of the experimental setup is shown in Figure 15. The unwanted contributions to the spectra (such as absorption of the glass substrate) from the reference sample are later subtracted out.[52] A substrate without a fabricated device is used as a reference cell to zero the instrument. [53]

The transmittance and absorbance spectra obtained employing this technique are often used to determine the transparency and the band gap of the material respectively. One of the deterministic factors for the solar cell's performance is that the light be transmitted and not be reflected by the layers. Hence, the transmittance data is a clear indicator of whether the HTL is capable of transmitting the incoming light.

This work focuses on comparing the obtained transmitted spectrum with that of current literature. Moreover, the absorbance spectra obtained from the experiment was used to roughly compare the band gap of the HTL to expected values from the literature. ITO and PTAA samples were analyzed and compared to the absorbance and transmission spectra in the range of 300-900nm. A Shimadzu UV-2501 was used to perform these measurements.

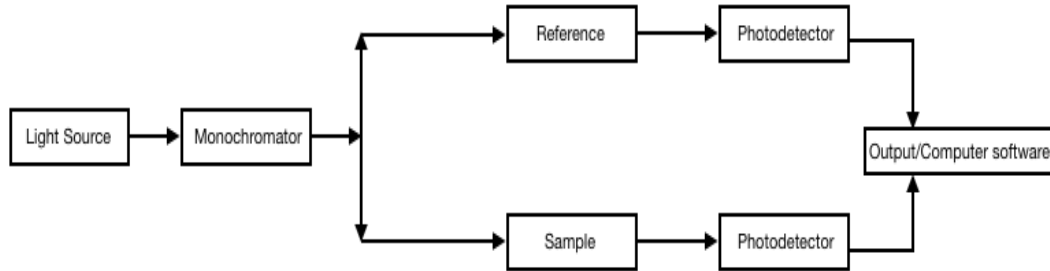


**Figure 15: Block diagram of UV-Vis setup**

## 2.5 Current-Voltage (J-V) Measurements

To determine the parameters in a solar cell such as the PCE, open circuit voltage, short circuit current, and maximum power point, the current-voltage (J-V) characteristics have to be measured under solar illumination. To perform this electrical characterization technique, an Oriel ABA sun simulator with AM 1.5G filter is used. The simulator provides  $100\text{mW}/\text{cm}^2$ , which is also known as 1 sun. The sample is connected to a Keithley 2400 source meter to measure current density (J) versus voltage (V). The voltage was scanned from  $-0.2\text{V}$  to  $1.1\text{V}$ . These measurement parameters were set using a LabView program, which also returned the values for PCE, open circuit voltage ( $V_{OC}$ ), short circuit current ( $J_{SC}$ ) and fill factor with an array that had the measured J-V values.

## 2.6 External Quantum Efficiency Measurements

External Quantum Efficiency (EQE) is used to effectively determine the device performance at a specific wavelength. A monochromator enables the filtering of light to have only one specific wavelength at an instance, while the short circuit current is measured. The data from EQE can be used in conjunction with J-V measurement to gain more insight about the device and confirm the performance standards. Generally, EQE is defined as the ratio of converted electrons to the incoming number of photons that strike

a solar cell. Mathematically, at specific wavelength, the EQE is given by:

$$\begin{aligned}
 EQE(\lambda) &= \frac{\text{electrons out } (\lambda)}{\text{incident photons } (\lambda)} \\
 &= \frac{J_{sc}(\lambda)}{q\Phi(\lambda)} \\
 &= \frac{hc}{q} \cdot \frac{J_{sc}(\lambda)}{\lambda \cdot P_{in}(\lambda)} \\
 &= 1240 \cdot \frac{J_{sc}(\lambda)[Acm^{-2}]}{\lambda[nm] \cdot P_{in}(\lambda)[W cm^{-2}]} \quad (8)
 \end{aligned}$$

where  $\Phi$  is the photon flux,  $P_{in}$  the light intensity at certain wavelength  $\lambda$ ,  $q$ ,  $h$  and  $c$  being elementary charge, Planck's constant and the speed of light respectively.[54]

A Xenon light source is used to create a light beam which is passed through sorting filters and a monochromator, resulting in monochromatic light beam. This monochromatic light beam is focused on the device. The monochromator scans over a range of wavelengths, from 400-900nm. The experimental setup used to perform this measurement is shown in Figure 16.

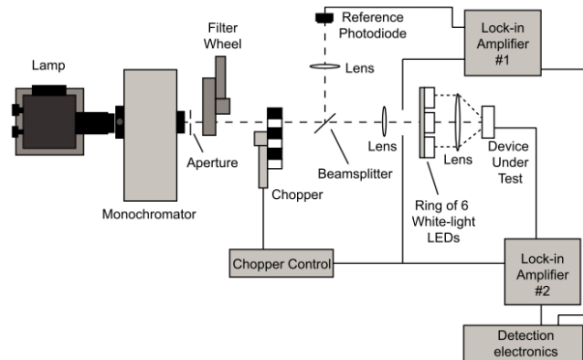


**Figure 16: Schematic diagram of EQE measurement setup [55]**

## **2.7 Temperature and Light Intensity dependent measurements**

Light intensity and temperature dependent characterization of solar cells fabricated in this work were done using an ARS Closed Cycle Nanoscience probe station PS-CC-NS. Besides for temperature and light dependent studies, this tool was also used to study the light soaking effects and electrical stress effects in the solar cells. The equipment is integrated with a sample stage, source meter, cryocooler, vacuum chamber, light source, and an impedance analyzer. The system was operated using a python code.

The light intensity was varied using neutral density (ND) filters from  $1 \times 10^{-3}$  mW/cm<sup>2</sup> to 56.6 mW/cm<sup>2</sup>. The effect of light soaking upon current - voltage and electrical biasing was studied using a Keysight B2912A source measure unit.

## **2.8 Energy dispersive X-Ray Spectroscopy**

Energy dispersive x-ray spectroscopy (EDS) is a characterization technique that reveals the elemental composition of a sample. This is done by the detection of x-rays emitted from the sample when bombarded by an energetic electron beam. The identification of an element is possible as each element has its unique characteristic x-ray spectra. This technique is used to measure the atomic ratio and prove the elements that were suspected to be in the sample. In this work, EDS will be used to see if any chemical change has occurred in the sample after light soaking and electrical poling (application of electric field).

An FEI Helios NanoLab 400 DualBeam field emission scanning electron microscope (SEM) was used.

### 3. RESULTS

Now that the characterization methods have been introduced the first step in this section is to characterize the Hole Transport Layer, PTAA, for its thickness which results in the best device performance. Surface profilometry technique was used to determine the thickness of the HTL of samples of various concentrations of PTAA spun on ITO. The same samples were characterized by AFM to determine the roughness. UV- Vis spectroscopy was used to study the absorbance and transmittance of the HTL and to calculate the band gap of the material. The UV-Vis spectra were compared to the results found in literature. Upon these preliminary investigations, the J-V curve of the champion device were utilized to study different performance parameters using the Two-Diode model. The HTL with best performing parameter was used to study the temperature dependent stability of the device.

#### 3.1 Surface profilometry of the Hole Transport Layer

The stylus profilometer was used in this work to determine the thickness of the PTAA HTL. PTAA powder bought from a commercial vendor was dissolved in toluene to make solutions of 2,3 and 4 mg/ml which were spun using the recipe as described in device fabrication section. The data from profilometer should provide insight about how varying the concentration has an impact on the thickness of HTL.

The average thickness for the samples with error bars which is indicative of measurement deviations is shown in Figure 17 with appropriate error bars which indicates the deviation. We can see that the data exhibits a trend when the concentration of the solution is varied with a constant spin speed. For the PTAA samples, there is a

linear increase in thickness with increasing concentration. The average thickness for solution of 2mg/ml, 3mg/ml and 4mg/ml are found to be  $8.5\pm 0.8$  nm,  $15.4\pm 0.7$  nm and  $24.8\pm 0.9$  nm respectively.

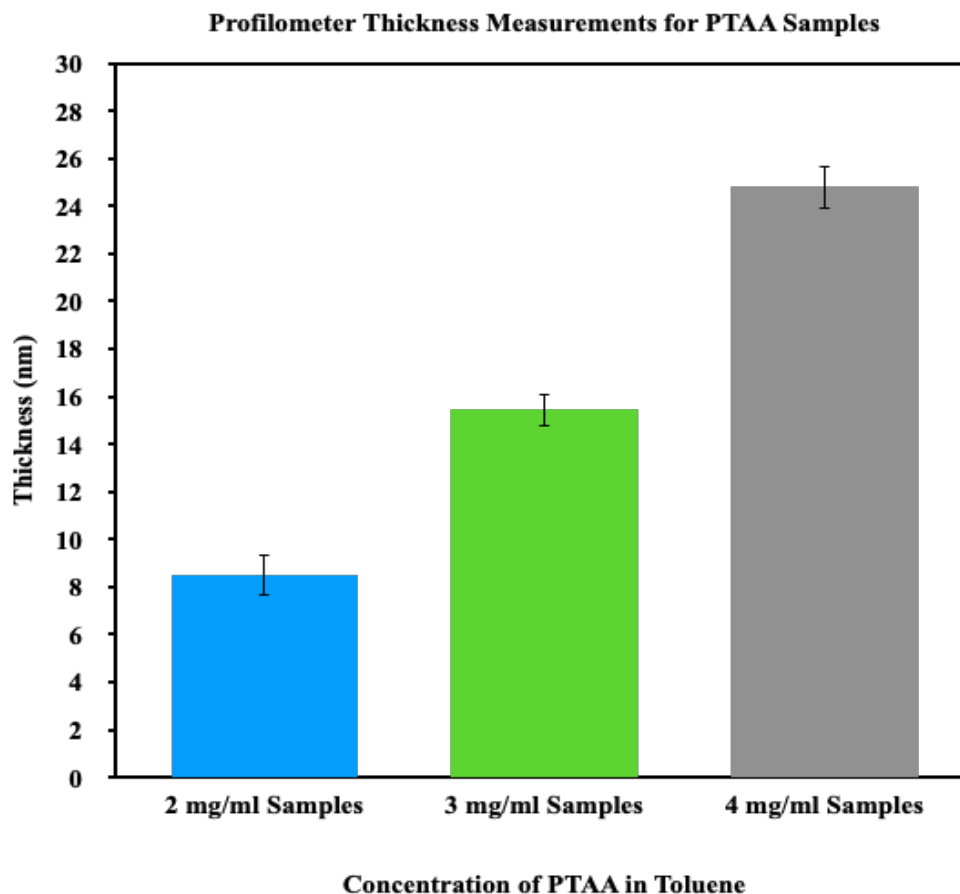


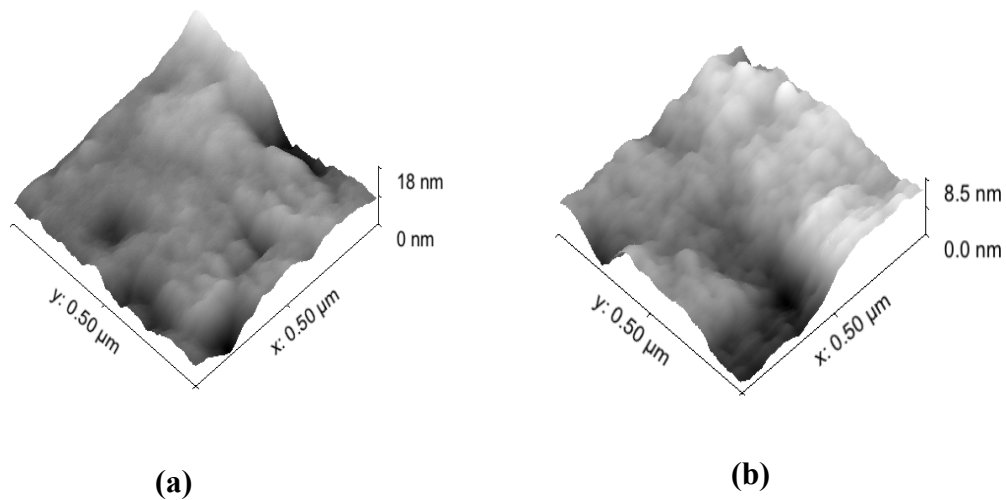
**Figure 17: Profilometer results with average thickness for PTAA samples of different thickness**

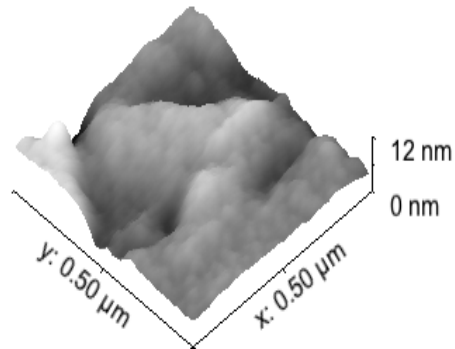
Even though a concentration of 1.5mg/ml PTAA was used to study the PCE variation with concentration, it was not used in metrology measurements as the cutoff thickness of profilometer is 8 nm and the thickness of 2mg/ml concentration solution is right at the borderline of that limit. Moreover, an extrapolation of the thickness data was done to predict the thickness for 1.5 mg/ml which also suggested that the thickness lies

below the cutoff limit of a profilometer. Hence, the study of variation of thickness for concentrations below 2 mg/ml of PTAA using a profilometer does not lie within the limit of the instrument itself. So, a further comprehensive study regarding the variation of thickness, for different concentration, with spin speed requires further methodical study which was out of the scope of this work.

### 3.2 Atomic Force Microscopy of the Hole Transport Layer

This work will utilize the basic tapping mode in AFM to investigate the roughness and image the PTAA HTL of various concentration. The images of PTAA in toluene spun onto ITO substrates using optimized process parameters were taken to compare the roughness for different solutions. The images can be seen in Figure 18.





(c)

**Figure 18: AFM images of PTAA HTL with precursor solution concentrations (a) 2, (b) 3, and (c) 4 mg/ml**

The images by AFM were lateral square in shape with a dimension of  $0.5 \mu\text{m} \times 0.5 \mu\text{m}$ . The PTAA thin films had a random and rough sponge like texture which was revealed by AFM images. The parameters extracted from the AFM were the samples vertical displacement,  $R_{max}$  and the root mean square roughness,  $R_q$ . To have a uniformity in sample type the same samples from profilometer were included in the sample population. The maximum vertical displacement and the root mean square roughness for the samples is shown in Figure 19. The vertical displacement ranged from 8.5nm to 12 nm whereas the root mean square roughness was in the range of 1.59 to 2.13 nm.

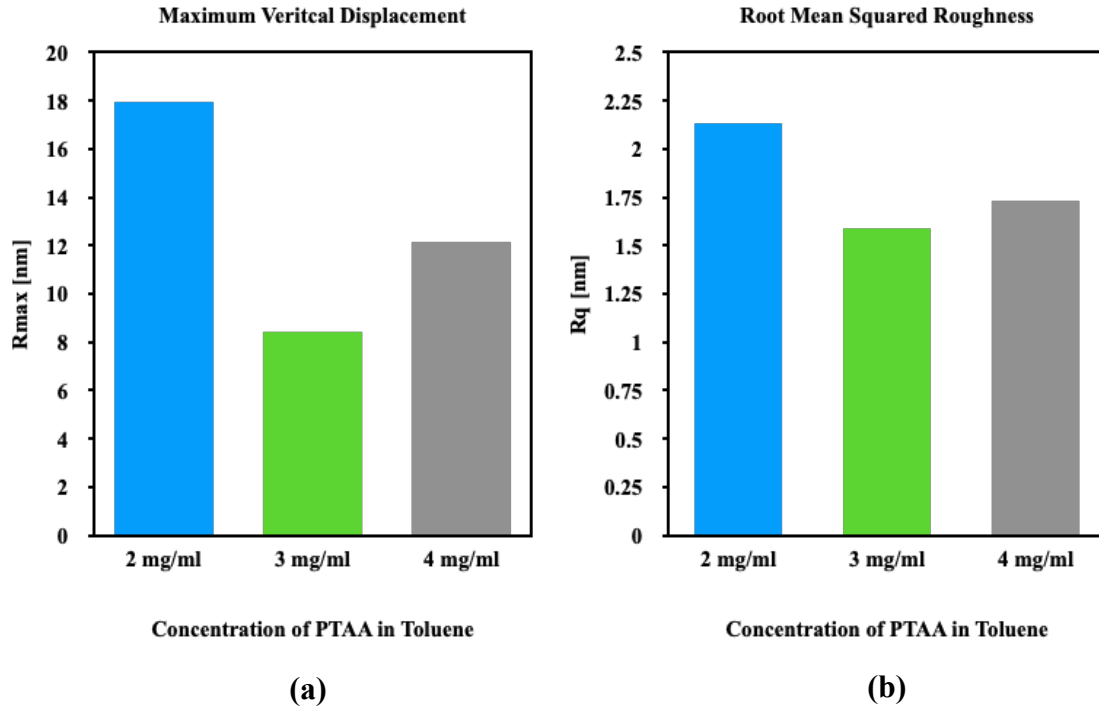


**Figure 19: Bar graphs of (a) root mean square roughness, and (b) vertical displacement of PTAA in toluene**

### 3.3 Ultraviolet-Visible Spectroscopy of the Hole Transport Layer

The transmittance spectra of 2 mg/ml PTAA on Glass/ITO is shown in Figure 20. The reference sample was bare glass/ITO which is subtracted by the software to obtain the spectra of only PTAA thin film. It can be seen that PTAA has a maximum optical transmittance around 90% at 425 nm which decreases to around 60% . We can also notice that the transmittance curve has characteristic wrinkles at 390 nm, 430 nm.

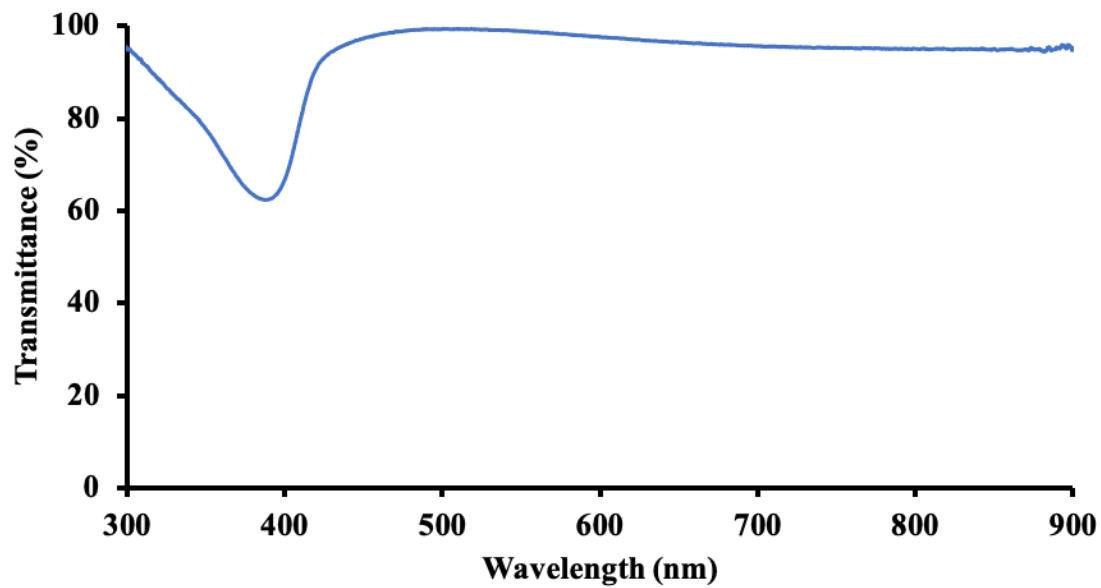


**Figure 20: UV-Vis transmittance spectra for PTAA on glass/ITO**

The absorbance spectra for 2 mg/ml PTAA on glass/ITO is shown in Figure 21. We can notice that there is a distinguishable characteristic peak at around 384 nm. This peak also corresponds to the peak in the transmittance spectra as in Figure 20, which is also the absorption onset at around 384 nm. Using this absorption onset, the bandgap of PTAA was found to be 3.22 eV which is close to the value found in literature. [56]

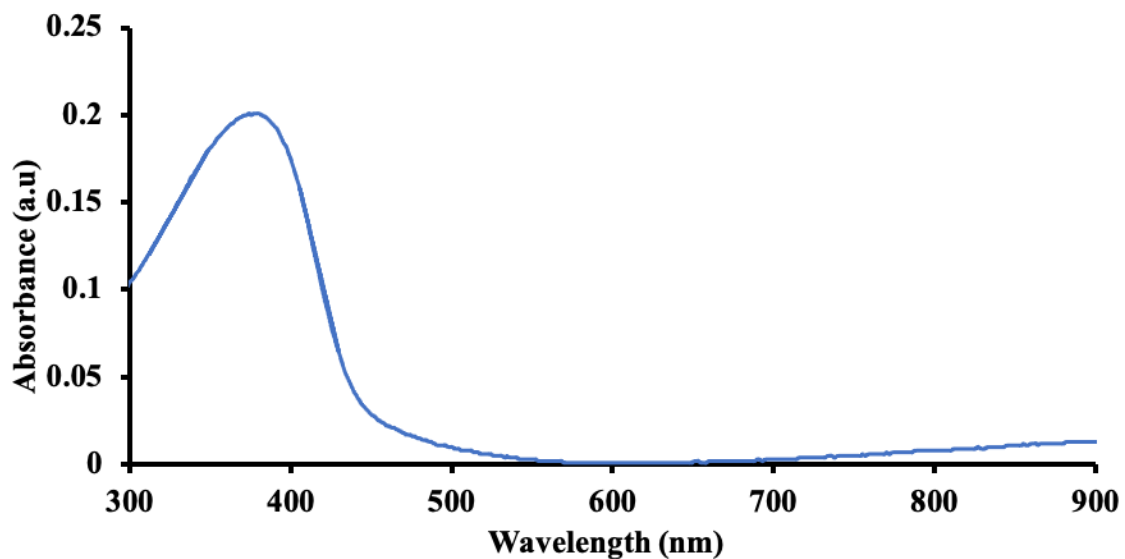


**Figure 21: Absorbance spectra for PTAA on glass/ITO spectra to calculate bandgap**

As the preliminary characterization for the HTL is describes in the previous sections, now this work will move on to the electrical characterization of the perovskite solar cell with PTAA as the HTL. After that, this thesis will describe the investigations of the stability of solar cells of the aforementioned architecture with PTAA as HTL upon varying temperature.

### 3.4 Current-Voltage (J-V) Measurements

This section focuses on characterizing a working photovoltaic device with PTAA as HTL. The details regarding the characterization method are as mentioned in the methods section. The results include J-V curve for the devices alongside the different performance parameters. Forward and reverse current voltage sweeps at a rate of 0.1 V/s were obtained for the solar cell under AM1.5G simulated solar illumination to obtain values for PCE, FF,  $J_{sc}$  and  $V_{oc}$ . All the devices fabricated to study the PCE variation with thickness were tested in ambient conditions.

The J-V curve for the champion device with the architecture glass/ITO/PTAA/CH<sub>3</sub>NH<sub>3</sub>PbI<sub>3</sub>/C<sub>60</sub>/BCP/Al is shown in Figure 22. We can see that there is no noticeable hysteresis between the forward and reverse sweep. The PCE for the forward sweep is 17.75% and that for reverse sweep is 17.64% with an average of 17.7%. The FF is also almost equal for forward and reverse sweep 80.08% and 79.14% respectively. The current density,  $J_{sc}$ , for forward and reverse sweeps were -21.32 mA/cm<sup>2</sup> and -21.43 mA/cm<sup>2</sup> respectively. The open circuit voltage however is equal for both forward and reverse sweeps with a magnitude of 1.04 V. This champion device had a PTAA concentration of 2 mg/ml which, when spun onto the ITO with the optimized recipe discussed in device fabrication section, led to a PTAA film thickness of ~8nm PTAA film. There was a variation in performance parameters when the concentration of PTAA in toluene was changed to vary the thickness of the PTAA HTL layer. A statistical variation of the performance parameters will be discussed in the following subsection.

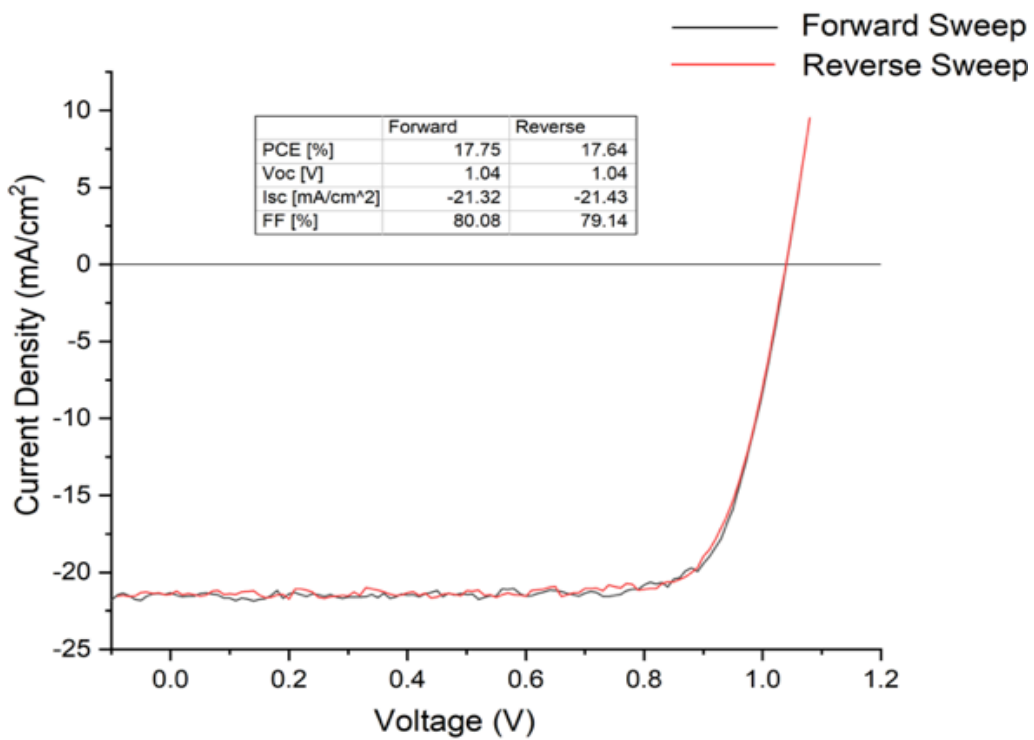


Figure 22: J-V curve for champion device with 2mg/ml concentration of PTAA HTL

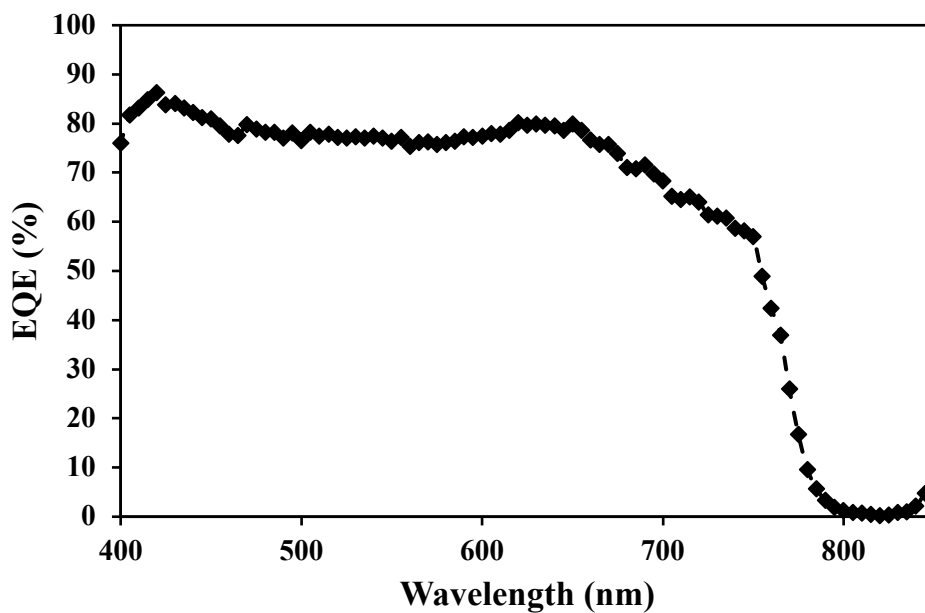
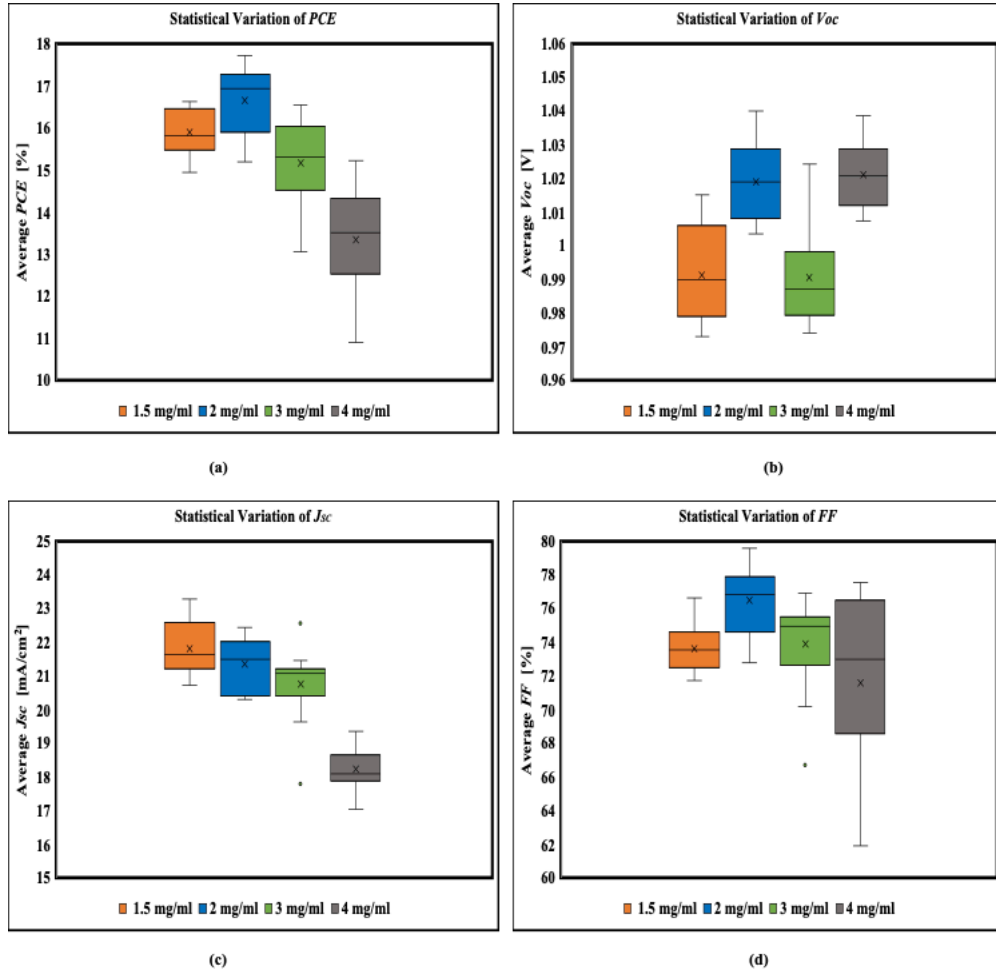


Figure 23: External Quantum Efficiency of a perovskite solar cell with 2mg/ml concentration of PTAA HTL

The external quantum efficiency was measured to investigate the wavelength dependent performance of the solar cell with PTAA HTL. The EQE was measured from a solar cell device with a PTAA HTL of 2 mg/ml was used to fabricate the solar cell to measure its EQE. The EQE is almost 80% in the range of 400nm to 750nm. The result is shown in Figure 23. The integrated current density from the device had the same trend as shown in Figure 22. However, a difference of ~8% was calculated which might be because of the spectral mismatch of the lamp used in the EQE setup or because of the resistance of the current preamplifier used in the EQE setup.

### **Statistical Variation in Performance Metrics**

For each concentration of PTAA, 1.5 mg/ml, 2 mg/ml, 3 mg/ml and 4 mg/ml, 16 devices were made. As the main focus was to optimize the PTAA HTL for the aforementioned device architecture, only the thickness of the PTAA HTL was changed with the use of different concentrations of the PTAA. Before the optimization process, the devices lacked in performance which was due to issues with the RPM during spin coating that led to uneven substrate coverage. After finally having a spin recipe that deposited PTAA layer evenly onto the substrate with almost no visible defects such as pinholes, the performance metric of the devices improved. Then, a sample population for devices was acquired with the optimized process parameters for various concentration of PTAA HTL. The statistical variation of device parameters with the variation in concentration is shown in Figure 24.



**Figure 24: Statistical variation of performance metric for devices with different process parameters (a) PCE (b)  $V_{oc}$  (c)  $J_{sc}$  and (d) FF**

As seen from the figures above using PTAA with a concentration of 2 mg/ml show better performance under standard testing conditions. The J-V curves from each sample was used to calculate the device parameters, including PCE, FF,  $J_{sc}$  and  $V_{oc}$  which are tabulated in Table 2.

**Table 2: Performance metric averages for solar cell samples with PTAA HTL of different concentrations**

<b>Device performance metrics with varying concentration of PTAA</b>				
<b>Concentration of PTAA in Toluene</b>	<b>PCE [%]</b>	<b>V<sub>oc</sub> [V]</b>	<b>J<sub>sc</sub> [mA/cm<sup>2</sup>]</b>	<b>Fill Factor [%]</b>
<b>1.5 mg/ml</b>	<b>15.89 ± 0.57</b>	<b>0.99 ± 0.01</b>	<b>-21.78 ± 0.78</b>	<b>73.59 ± 1.35</b>
<b>2 mg/ml</b>	<b>16.64 ± 0.77</b>	<b>1.01 ± 0.01</b>	<b>-21.35 ± 0.78</b>	<b>76.48 ± 1.97</b>
<b>3 mg/ml</b>	<b>15.21 ± 1.05</b>	<b>0.99 ± 0.01</b>	<b>-20.73 ± 1.11</b>	<b>73.88 ± 2.81</b>
<b>4 mg/ml</b>	<b>13.40 ± 1.19</b>	<b>1.02 ± 0.01</b>	<b>-18.23 ± 0.63</b>	<b>71.60 ± 5.19</b>

Devices with a 1.5 mg/ml PTAA had an average PCE of 15.89±0.57%. Despite having low deviation, the maximum PCE from this sample was below the champion device made with a concentration of 2 mg/ml PTAA concentration. Also, the devices with 2 mg/ml PTAA HTL had a PCE greater than 15% in all the cases and approached to a maximum of 17.75% for the champion device. Moreover, the V<sub>oc</sub> and FF were consistently greater than or equal to 1V and 74% respectively in the case of devices with 2 mg/ml PTAA concentration. The average FF and V<sub>oc</sub> for devices with PTAA HTL of 1.5 mg/ml concentration were 73.59±1.35% and 0.99±0.01V respectively. This high magnitude in FF can be attributed to the devices having low shunt resistance. The parameters including the one mentioned on this section and parameters such as ideality factor, diode current, shunt and series resistance using a two-diode model will be discussed in the next section.

Due to some unavoidable defects that were introduced to the device during processing, some of the devices failed, leading to no output at all. Besides having no output, some of the parameters from devices were outliers and were not included in the

statistical analysis. The defects were mainly caused during spin coating, contamination by particles, or were shorted whilst applying silver paint after encapsulation. Also, as there was no control over the encapsulating robot due to which some of the encapsulating caps came off the devices. These devices were not incorporated in the statistical analysis presented above. Hence, for sample group for 1.5 mg/ml, 2 mg/ml, 3 mg/ml and 4 mg/ml, 14, 12, 13, 13 of 16 devices were ultimately included in the sample population respectively. Out of total 80 solar cell fabricated; 12 samples were excluded. The ideality factor and the resistances for the device will be obtained with a two-diode model in the next subsection.

### **Two-Diode Modeling to find resistance and ideality factor**

Solar cell parameters such as the Fill Factor, Power conversion efficiency, Open-circuit voltage, and Short circuit current can be directly observed from the measured J-V curve without having to do any calculations. However, certain parameters such as the shunt resistance,  $R_P$ , series resistance  $R_S$  and the ideality factor  $n$  cannot be directly read from the J-V curve without performing model calculations. These parameters are internal to the device and arise due to the interface between various layers and the materials used to make up the solar cell. The J-V curves of the devices fabricated for this work will be fit using a two-diode model. This work will utilize a standalone executable program in MATLAB that was published by *Suckow et al.* [42] to calculate shunt resistance, series resistance and ideality factor from the measured J-V curves. This program utilizes a classical gradient based numerical approach.

The diode equation mentioned in the introduction section is what will be fitted using

this method. But, instead of solving the transcendental equation, the program transforms the equation to find the correct value of  $J$  as the root of the function  $f$ :

$$f(V, J) = J_{ph} - J - \frac{V + JR_S}{R_p} - J_{01} \left( e^{\frac{q(V + JR_S)}{n_1 k_B T}} - 1 \right) - J_{02} \left( e^{\frac{q(V + JR_S)}{n_2 k_B T}} - 1 \right) = 0 \quad (9)$$

The  $f(V, J) = 0$  is only true for the correct value of  $J$  at every voltage which will be determined with the software. Along with  $J$ , the shunt resistance,  $R_p$ , series resistance,  $R_s$ , and the ideality factors will also be calculated. There were some procedures that needed to be followed in order for the software to take in the data and enabled the fitting of the various parameters of interest. Firstly, the data obtained from the Oriel solar simulator were converted from Amperes/cm<sup>2</sup> to Amperes and arranged in a column of reverse values of voltage versus the current. Secondly, the file was imported to the program and the area of the solar cell and the room temperature of 0.0625 cm<sup>2</sup> and 24° C was included in the model. Due to the complexity of the calculation of various parameters the software resulted in incorrect or unusual values of ideality factor to blow up to 100 or more. But, only values of 1, 2 or 3 successfully explains the recombination mechanisms in a perovskite PV cell.[57] So, to avoid that, a methodical approach[58] was considered described below.

A single diode was fitted first without using any series or shunt resistance. The resulting value of the current through the single diode was used as a guess value to float the series and shunt resistance. Then, the series and shunt resistance and the current through the single diode was used to float all other parameters including the current

through the second diode. It should be mentioned that the ideality factor through the first diode was fixed as 1 and that of diode 2 was guessed as 2 considering various injection scenarios in practical devices.[59] The J-V curves obtained for solar cell made with PTAA HTL of various concentrations were used to estimate the shunt resistance, the series resistance, and the ideality factor. This approach obtained the deviation and averages in the determined parameters that were used in the modeling. The parameters obtained using this model are tabulated in Table 5. The short circuit current density obtained by fitting the model were close enough (difference of not more than 0.05%) to the values obtained during the measurement of the solar cells used in this work. Besides the short circuit current, the model also gave the PCE,  $V_{OC}$  and FF which were in close agreement with that of the values in Table 2.

The J-V curves of each concentration's champion device in the architecture of glass/ITO/PTAA/MAPI/ $C_{60}$ /BCP/Al with the parameters during measurement are shown starting in Figure 25 with the concentration of 1.5 mg/ml PTAA. Ideality factors, series and shunt resistances for the population were calculated by fitting the two-diode model. The PCE,  $V_{OC}$ ,  $J_{SC}$  and FF were measured to be 16.55%, 0.98V, -22.50 mA/cm<sup>2</sup> and 74.62% respectively. The parameters  $J_{PH}$  from two-diode model was found to be -22.55mA/cm<sup>2</sup> which is close to the value measured. The diode model also resulted in the shunt and series resistances of 4.98k $\Omega$ •cm<sup>2</sup> and 4.55 $\Omega$ •cm<sup>2</sup> respectively. The parameters

obtained using the modeling is tabulated in Table 3.

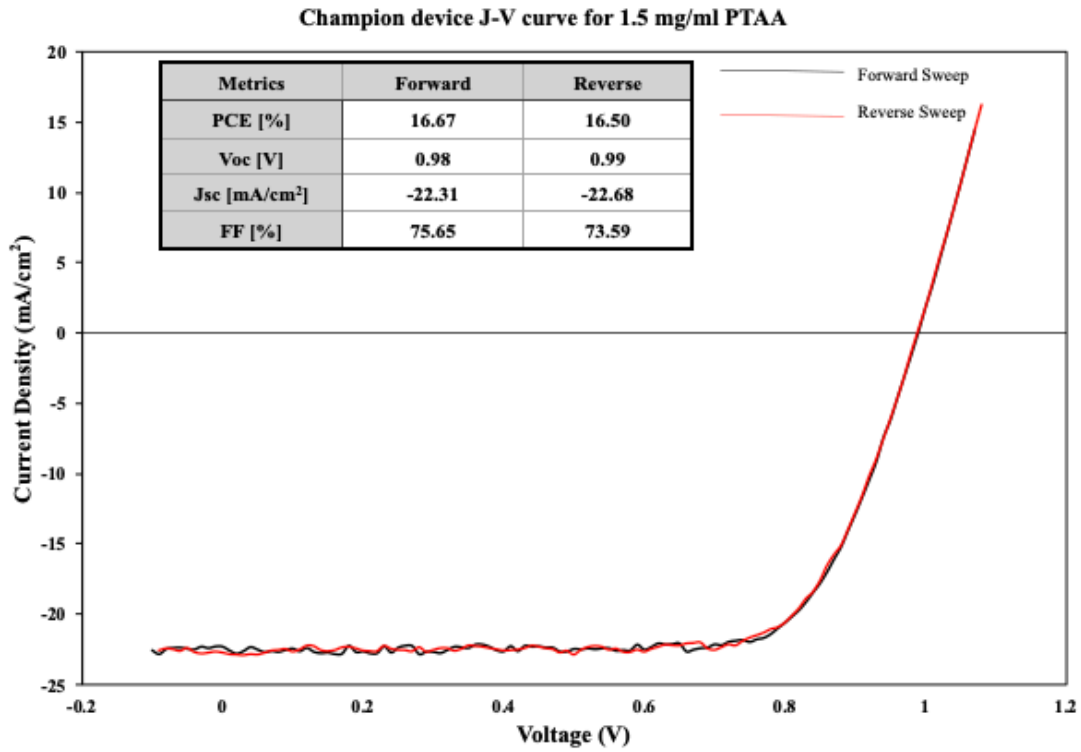


**Figure 25: J-V curve for champion device with 1.5 mg/ml concentration of PTAA**

**Table 3: Two-Diode model fit parameters for champion device of 1.5mg/ml concentration of PTAA**

$J_{PH}$ [mA/cm <sup>2</sup> ]	$J_{01}$ [mA/cm <sup>2</sup> ]	$J_{02}$ [mA/cm <sup>2</sup> ]	$n_1$	$n_2$	$R_P$ [k $\Omega$ •cm <sup>2</sup> ]	$R_S$ [ $\Omega$ •cm <sup>2</sup> ]
-22.55	$2.06 \cdot 10^{-16}$	$4.79 \cdot 10^{-8}$	1	2	4.98	4.55

Devices having 2 mg/ml concentration of PTAA had the best performing metric. The champion device an average PCE of 17.64%. Moreover, the  $V_{OC}$  and FF for the champion device was 1.04 V and 80%. The high magnitude of the FF was evident by the shunt resistance of 5.07 k $\Omega$ •cm<sup>2</sup>. This high shunting resistance compliments the high FF.

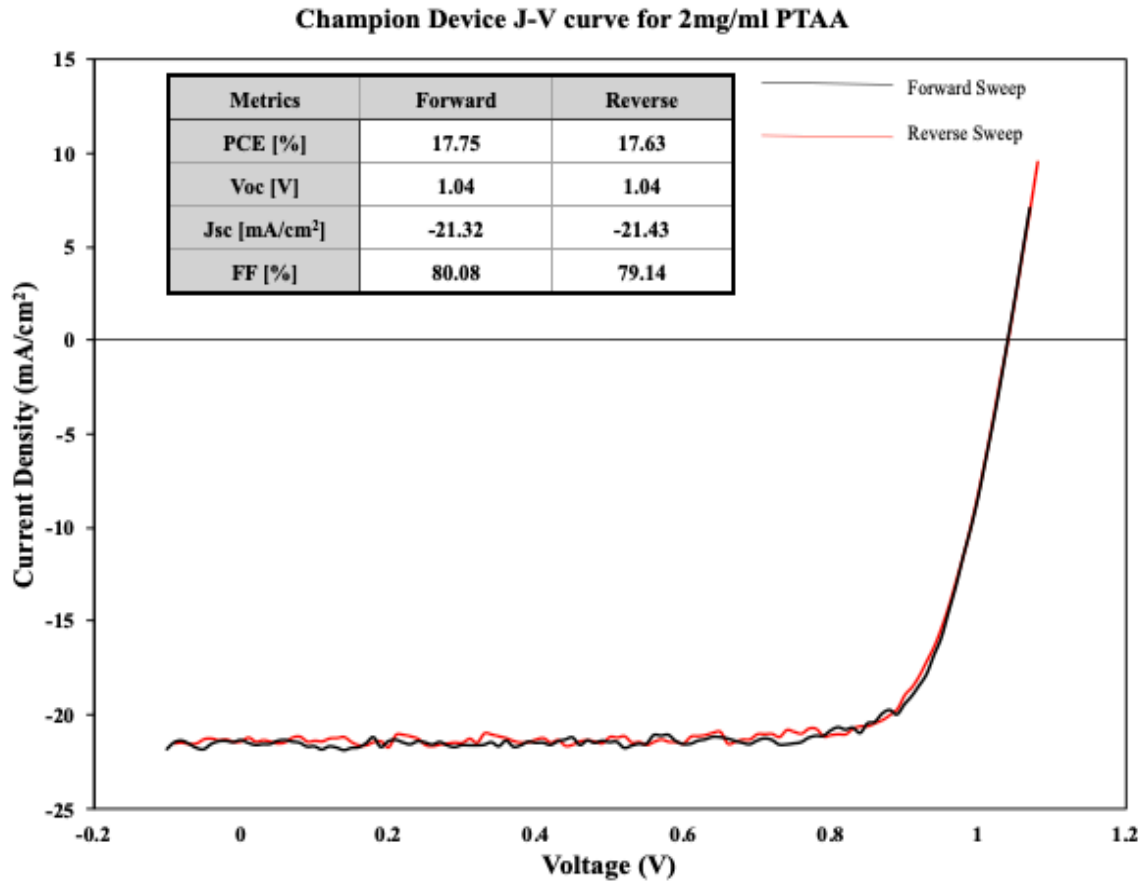


**Figure 26: J-V curve for champion device with 2mg/ml concentration of PTAA**

**Table 4: Two-Diode model fit parameters for champion device of 2mg/ml concentration of PTAA**

$J_{PH}$ [mA/cm <sup>2</sup> ]	$J_{01}$ [mA/cm <sup>2</sup> ]	$J_{02}$ [mA/cm <sup>2</sup> ]	$n_1$	$n_2$	$R_P$ [k $\Omega$ ·cm <sup>2</sup> ]	$R_S$ [ $\Omega$ ·cm <sup>2</sup> ]
-21.42	$5.36 \cdot 10^{-17}$	$7.65 \cdot 10^{-8}$	1	2.2	5.07	3.09

Similarly, parameters for champion devices with PTAA HTL concentration of 2 mg/ml, 3mg/ml and 4mg/ml used for this work were calculated using the two-diode model. The J-V curves with an inset of measured parameters and tabulated values of calculated ideality factor, shunt resistance and series resistance can be seen in Figure 25,

26 and 27 respectively. The series resistance seems to be increasing linearly with increase in concentration of PTAA. This might be the reason of decreasing PCE for higher concentrations than 2 mg/ml. The champion devices with 4mg/ml and 3mg/ml had low FF compared to 1.5mg/ml and 2mg/ml. This can be linked to the shunt resistance of 1.76  $k\Omega \cdot cm^2$  and 2.33 $k\Omega \cdot cm^2$  compared to 4.98 $k\Omega \cdot cm^2$  and 5.07 $k\Omega \cdot cm^2$  in case of champion devices with 1.5mg/ml and 2mg/ml respectively.

**Table 5: Two-Diode model fit parameters for perovskite solar cell with various PTAA HTL concentrations**

Device fit parameters with varying concentration of PTAA							
Concentration of PTAA in Toluene	$J_{PH}$ [mA/cm <sup>2</sup> ]	$J_{01}$ [mA/cm <sup>2</sup> ]	$J_{02}$ [mA/cm <sup>2</sup> ]	$n_1$	$n_2$	$R_P$ [k $\Omega \cdot cm^2$ ]	$R_S$ [ $\Omega \cdot cm^2$ ]
1.5 mg/ml	21.84 ± 0.77	1.89 ± 1.16 · 10 <sup>-16</sup>	3.88 · 10 <sup>-8</sup>	1	1.94 ± 0.18	5.82 ± 3.1	5.41 ± 1.15
2 mg/ml	21.42 ± 0.76	6.12 ± 5 · 10 <sup>-17</sup>	8.29 ± 0.18 · 10 <sup>-8</sup>		1.90 ± 0.33	2.61 ± 1.4	3.3 ± 0.8
3 mg/ml	20.7 ± 1.13	1.36 ± 1.04 · 10 <sup>-16</sup>	6.31 ± 3.07 · 10 <sup>-8</sup>		1.99 ± 0.01	5.93 ± 1.0	4.0 ± 0.1
4 mg/ml	18.5 ± 0.54	7.85 ± 0.11 · 10 <sup>-16</sup>	1.14 ± 1.97 · 10 <sup>-7</sup>		2.04 ± 0.11	1.3 ± 0.3	7.7 ± 3.2

**Champion Device J-V curve for 3 mg/ml PTAA**

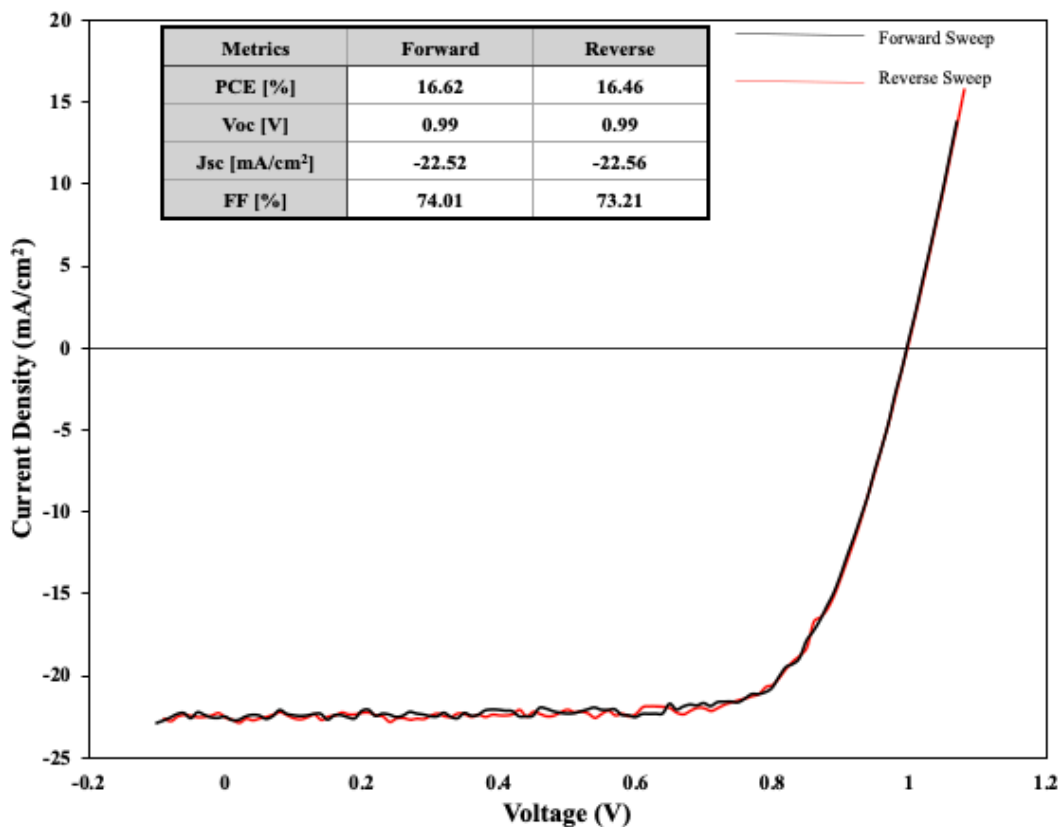


**Figure 27: J-V curve for champion device with 3 mg/ml concentration of PTAA**

**Table 6: Two-Diode model fit parameters for champion device of 3mg/ml concentration of PTAA**

$J_{PH}$ [mA/cm <sup>2</sup> ]	$J_{01}$ [mA/cm <sup>2</sup> ]	$J_{02}$ [mA/cm <sup>2</sup> ]	$n_1$	$n_2$	$R_P$ [k $\Omega$ ·cm <sup>2</sup> ]	$R_S$ [ $\Omega$ ·cm <sup>2</sup> ]
-22.58	$6.34 \cdot 10^{-17}$	$6.33 \cdot 10^{-8}$	1	2	2.33	3.87

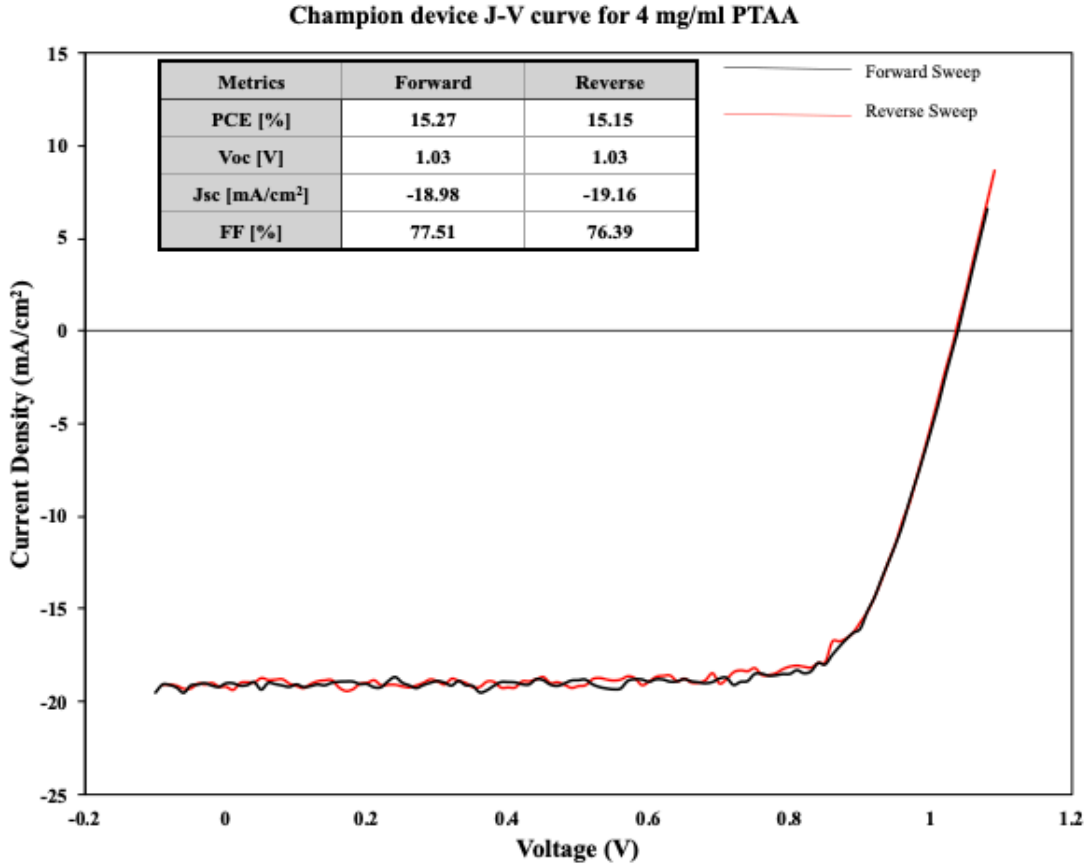


**Figure 28: J-V curve for champion device with 4 mg/ml concentration of PTAA**

**Table 7: Two-Diode model fit parameters for champion device of 4mg/ml concentration of PTAA**

$J_{PH}$ [mA/cm <sup>2</sup> ]	$J_{01}$ [mA/cm <sup>2</sup> ]	$J_{02}$ [mA/cm <sup>2</sup> ]	$n_1$	$n_2$	$R_P$ [k $\Omega$ ·cm <sup>2</sup> ]	$R_S$ [ $\Omega$ ·cm <sup>2</sup> ]
-19.10	$2.04 \cdot 10^{-15}$	$5.61 \cdot 10^{-8}$	1	2	1.76	5.07

### 3.5 Temperature and Illumination dependent measurements

Even though there is an upsurge in the PCE of perovskite PV devices since its introduction, there are certain challenges that persists with perovskite photovoltaic devices that currently hinder its commercialization. Researchers have shown that the degradation of hybrid halide perovskites is susceptible to its exposure to high humid

environments[60], exposure to ultra-violet light[61] and exposure to oxygen environments.[62] Moreover, temperature has also been a critical parameter that affects the performance of the device over time.[59] Temperature is mainly controlled during the fabrication process in solution processed perovskites in order to form a crystalline film and to evaporate the solvent that the perovskite is dissolved in. The hybrid perovskite, MAPI undergoes a phase change and chemical degradation which affects the performance of PV devices. The phase transition happens from orthorhombic ( $T < 165\text{K}$ ) to tetragonal ( $T = 165\text{ K to } 327\text{ K}$ ) to cubic ( $T > 327\text{ K}$ ) [60].

Recombination of the charge carriers has also been identified as being one of the main loss mechanism in photovoltaic devices and thus needs to be explored further to gain an understanding of the process that is likely to explain their underlying performance.[26] The temperature and light intensity dependent parameters of the solar cells including open-circuit voltage ( $V_{OC}$ ) and short-circuit current density ( $J_{SC}$ ) will be discussed below to gain a better understanding of the recombination mechanism.

This work will now investigate the PV performance whilst varying the temperature and intensity of illumination. Besides the PV performance, the phase transition of the perovskite will also be investigated by discussing the variation of open circuit voltage with temperature.

As a first step before starting the temperature and illumination dependent J-V study, the PTAA HTL based solar cells were measured at light under 1 Sun standard illumination condition using an Oriel ABA solar simulator which had an AM 1.5G filter installed and was calibrated to  $100\text{mW}/\text{cm}^2$ . The device parameters and the J-V curve at light and dark is shown in Figure 29. The  $V_{OC}$ ,  $J_{SC}$ , FF and PCE were 1.02 V, -

20.28mA/cm<sup>2</sup>, 76.74% and 15.94% respectively. Due to various processing conditions such as humidity inside the chamber during annealing the perovskite, contamination of samples during handling, cleanliness of the spin coater, it was challenging to achieve the parameters similar to that of the champion device. However, the best performing solar cell from the batch of 2mg/ml PTAA was chosen to do the temperature and illumination dependent study.

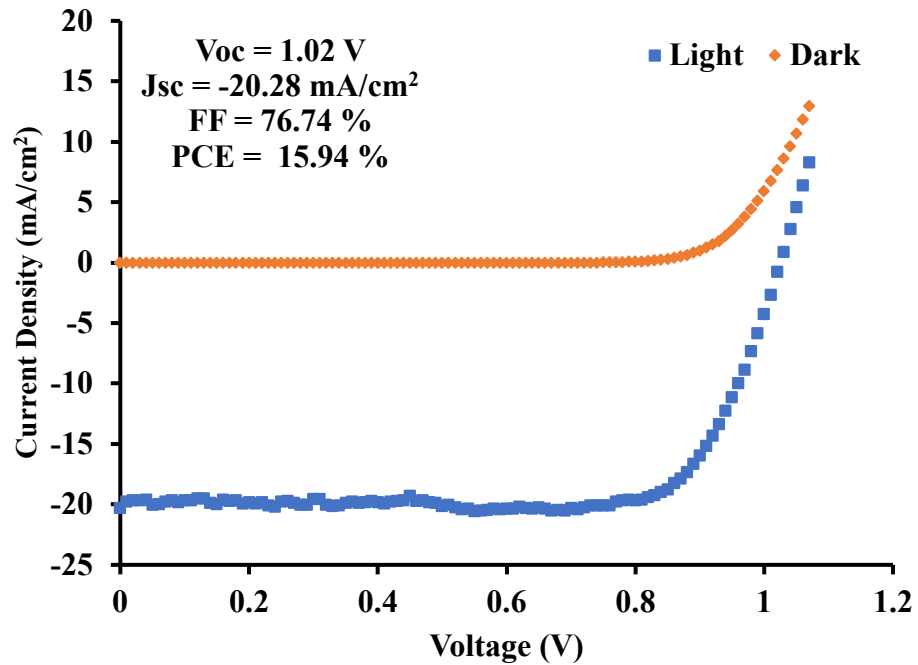


**Figure 29: The dark and illumination J-V characteristic of the PTAA HTL based perovskite solar cell with an inset of device parameters.**

The J-V characteristic for different illumination intensities is shown in Figure 30. The illumination was varied at room temperature from ( $8.71 \times 10^{-4} - 56.6$  mW/cm<sup>2</sup>). It was observed that the open circuit voltage was changing with a change in intensity of the illumination. The  $V_{OC}$  changed from 0.5V to 1V. Also, we can see that the short circuit current changes logarithmically with the change in intensity of illumination of light

source. We can note that the current density will not be equal to that in a solar simulator as the intensity was not varied to the standard intensity of  $100\text{mW}/\text{cm}^2$  because of the limitations of the instrument. As mentioned in the introduction section about the nature of open-circuit voltage, it was evident that it was linearly dependent on temperature change. The J-V characteristic of the solar cell with change in temperature at a fixed illumination is shown in Figure 31. The temperature was varied from 134 K to 374 K with an interval of almost 20 K. The interval was hard to maintain due to the sensitivity of the instrument which led to the temperature interval not being exactly 20 K. Temperature dependent measurement showed that the  $V_{OC}$  varied between 0.82 V ( $T = 134$  K) increasing to 1.02 V ( $T = 290$  K), decreasing, to 0.89 V ( $T = 374$  K). It is also evident from the graphs that the  $V_{OC}$  is dependent on illumination and temperature. However, no noticeable change in  $J_{SC}$  was observed as it was more prone to changing upon different illuminations. This anomalous change in parameter of the solar cell can be ascribed to the phase change of the perovskite which happens from orthorhombic ( $T < 165\text{K}$ ) to tetragonal ( $T = 165$  K to 327 K) to cubic ( $T > 327$  K). This change in open-circuit voltage with intensity and the volcano like distribution of open circuit voltage with changing temperature has been attributed to the phase change of the perovskite. [64]

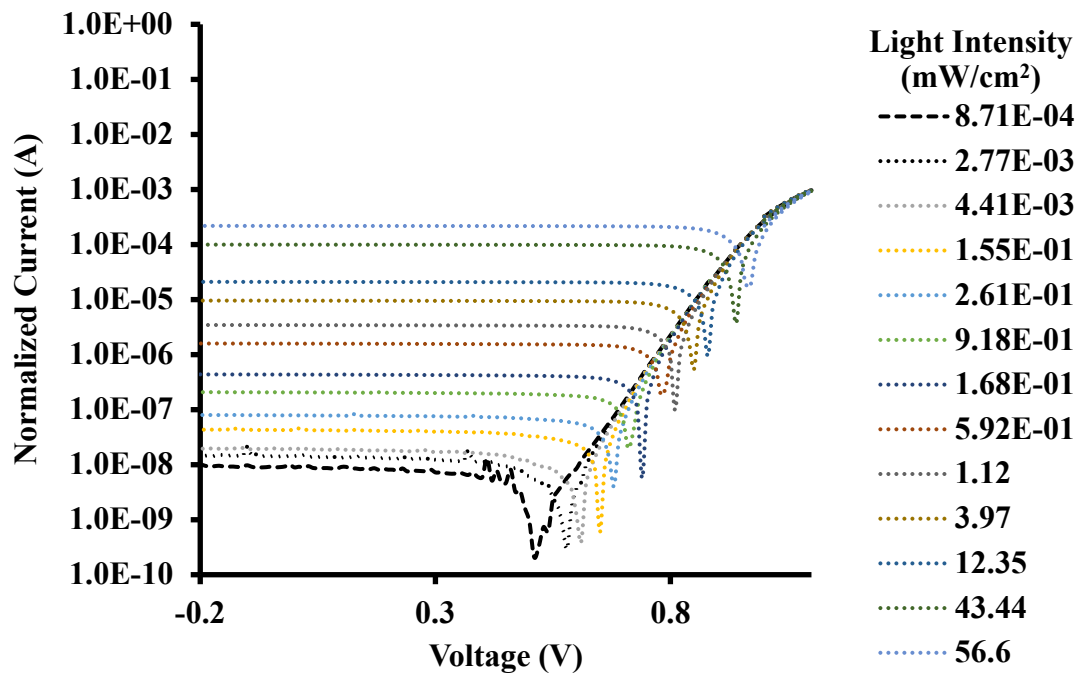


Figure 30: Intensity-dependent characteristic of PTAA HTL based PV cell

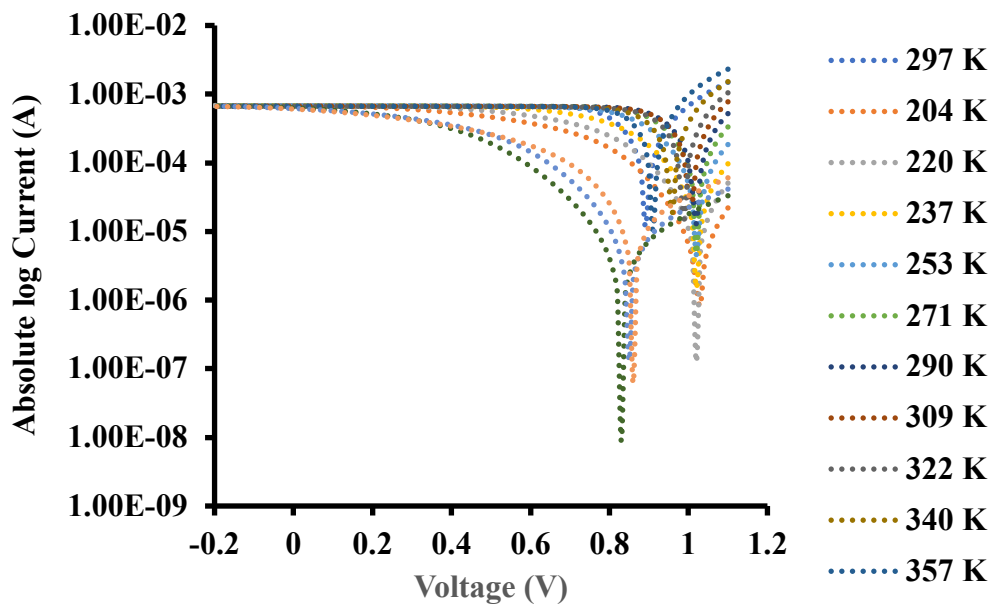


Figure 31: Temperature-dependent Current-Voltage characteristic of perovskite solar cell

### 3.6 Ion Migration in Hybrid Halide Perovskites

Besides degradation in humidity, oxygen environments and in ranges of temperature, hybrid halide perovskites have also been known to exhibit hysteresis in their J-V characteristic. This has been mainly attributed to the mobile charge carriers that are present intrinsically in the perovskite which migrate or cause interconversion of the hybrid perovskite MAPI to  $\text{PbI}_2$  and MAI when an electric field is applied.[65][66] This hysteresis was first reported by *Snaith et al.* and *Hoke et al.* when the J-V characteristic of the solar cell did not overlap with one another upon varying sweep speeds and directions.[67] This behavior has led to suggestions that the mobile ionic species inside the perovskite is the reason to cause hysteresis in the J-V measurements.

A photovoltaic cell is meant to function under sunlight. However, depending on the type of solar cell, there are different effects associated with exposure to light. The effect of light exposure on perovskite solar cells is mixed. There have been reports of degradation and recovery of the solar cell which results in hysteresis in J-V due to Ultraviolet light exposure. This mechanism has been explained by *Lee et al.* due to the generation, simultaneous passivation, and the neutralization of traps due to formation of  $\text{PbI}_2$ , which is formed while the perovskite degrades.[61] Due to the availability of equipment during the time of this research, the ARS probe station's lamp, equivalent to 0.7 suns, was used to study the behavior of the device fabricated in this work upon light exposure.

To investigate further if the devices fabricated for this work exhibit ion migration, a set of experiments were designed and executed with a methodical approach. It is necessary to mention that the change in the J-V curve is quite apparent due to the change

in normal shape of a J-V curve. The focus of this work now will not be to calculate and obtain the parameters associated with the device but will now shift towards exploring the reasons behind the S-shaped hysteresis in J-V characteristics. To start the experiment, a room temperature J-V acquisition was performed in full illumination of  $56.6\text{mW}/\text{cm}^2$ . The device showed a good  $FF$  and no noticeable hysteresis or shunting with a short circuit current of  $-13.6\text{mA}/\text{cm}^2$  and a  $V_{OC}$  of  $1\text{V}$ . After leaving the device in the dark for a few days in  $<10\mu\text{Torr}$  pressure the devices showed hysteresis and a prominent decrease in  $FF$  (about 40%) and the short circuit current. However, after exposure to light at full illumination of  $56.6\text{mW}/\text{cm}^2$  for about 20 minutes, the device showed regeneration in its  $FF$  and  $V_{OC}$  but a decrease in  $J_{SC}$ . This is shown in Figure 32. The forward sweep and the reverse sweeps showed noticeable hysteresis. To better visualize the result, only forward sweep was included in the plot. We hypothesize that this might be due to collisions between carriers which might cause the heating of the device and in turn causes loss in current. As this study was conducted in multiple steps, an overall reasoning behind the results will be done at the end of this section.

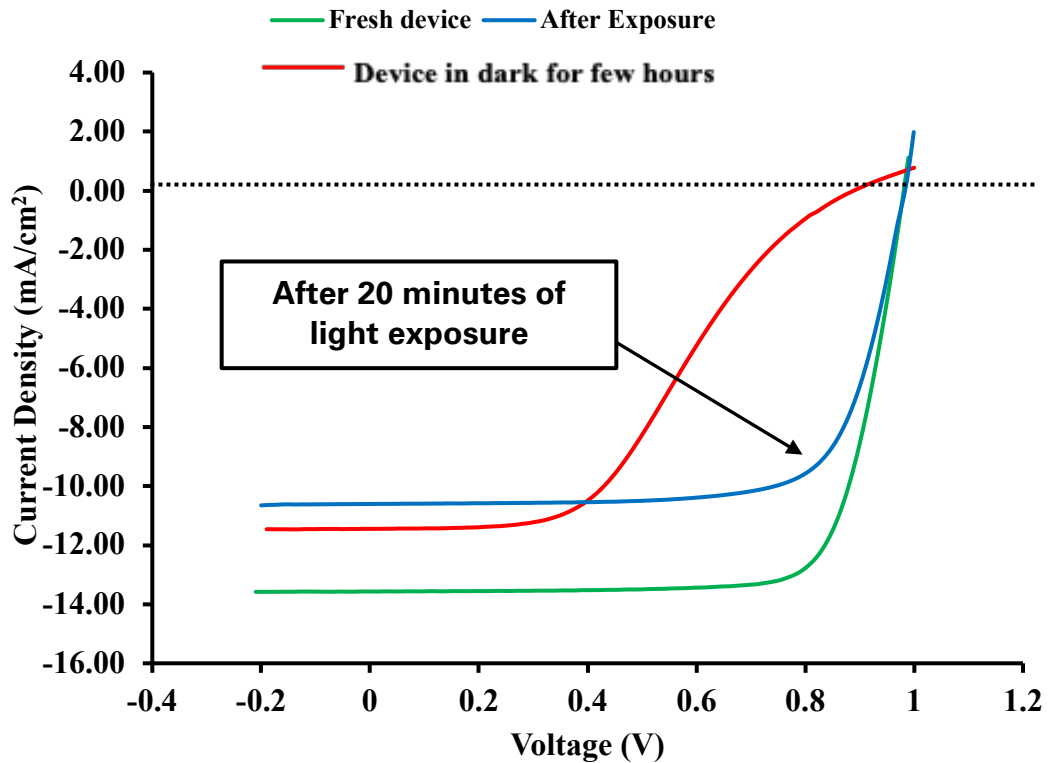


**Figure 32: Light induced recovery of J-V curve for solar cells with PTAA HTL**

To further investigate the sample, it was left close to the open circuit condition by biasing with +1V. To conduct this study, a different sample was taken which was also fabricated with the optimized process parameters. We had to use a new sample because the encapsulation of the prior sample fell off which led to device failure. Upon leaving the sample inside the vacuum in similar conditions for 42 hours, there was no noticeable change in the short circuit current density, but the device showed hysteresis in both sweeping directions and in its J-V curve, which dropped the *FF* of the device. Then, the device was biased at open circuit condition for 5 minutes which also led to the recovery of the device almost close to its initial conditions. This is shown in Figure 33.

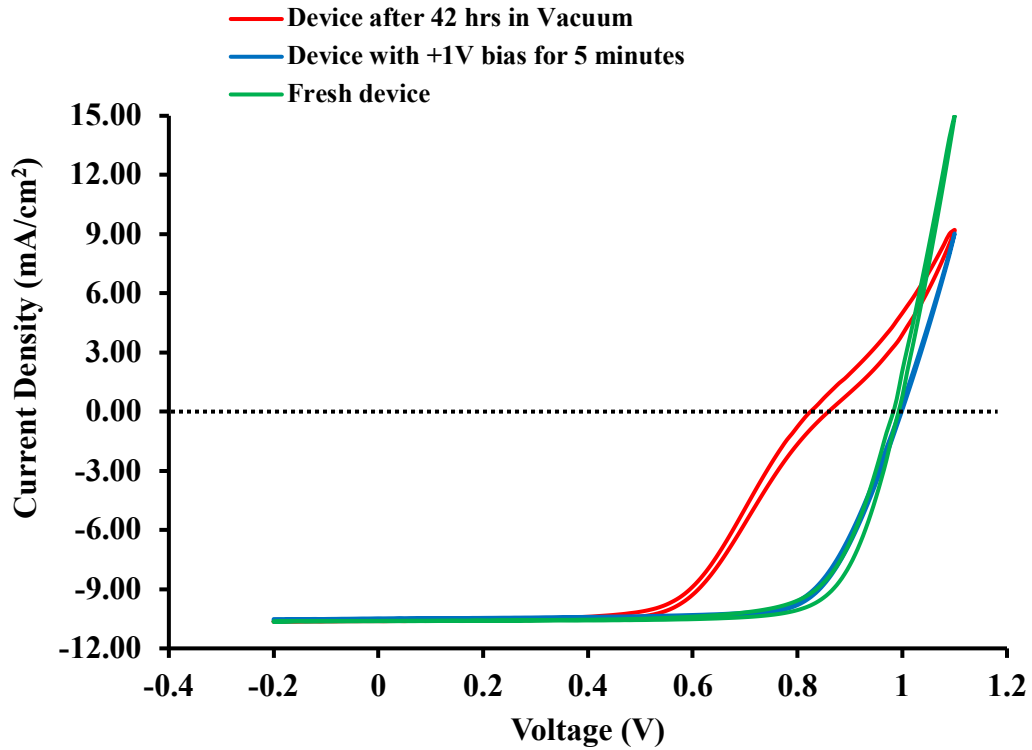


**Figure 33: Degradation and recovery of perovskite solar cells with PTAA HTL upon electrical bias**

Up to now, it is evident that the device fabricated in this work suffers from significant degradation when left in vacuum for a few hours and the degradation gets larger when left in vacuum for a few days. But this can be recovered either by light soaking or with an electric bias which seem to cause better regeneration of the device.

To see if mobile ions are causing this recovery due to electric biasing, a transient capacitance measurement was carried out for the devices. There is evidence that the change in capacitance in a device is related to the temperature and the movement of ions in either side of the terminal.[68][69][70] This approach was utilized in the devices fabricated in this work to study the change in capacitance. Capacitance transients, taken after a 1 volt , 1 second forward bias pulse immediately after each J-V measurement is

shown in Figure 34. The extraction of capacitance is based on a transient ion drift model where ions accumulate at the edge of depletion region with the influence of electric field.[71] Through these measurements, a high drop in capacitance is observed specially at temperature <300K.

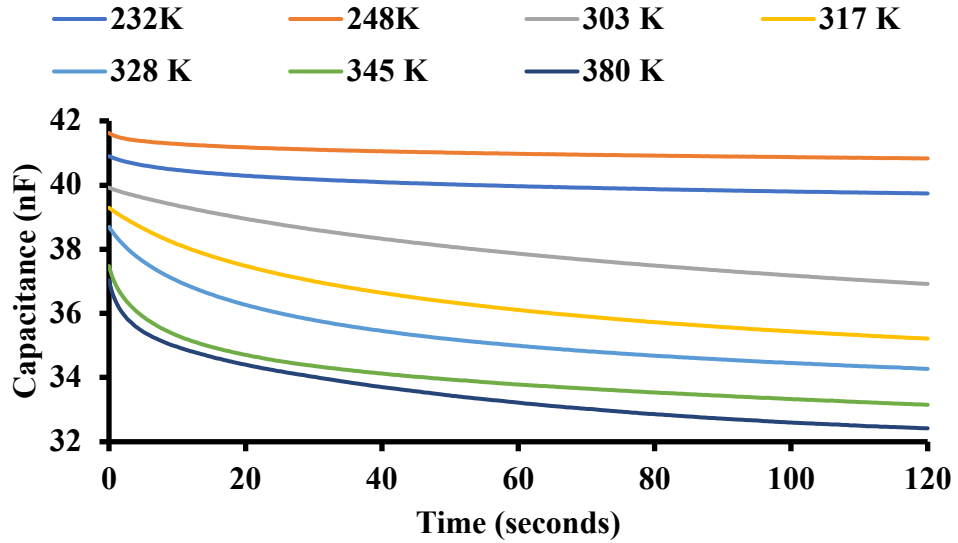


**Figure 34: Capacitance transient after +1V pulse for devices with PTAA HTL**

It should also be noted that the change in capacitance decreases with temperature. Now that these results have been obtained, this work will now focus on addressing the underlying mechanism. Previous works have shown that the hybrid halide perovskite MAPI is an ionic conductor. The ions that constitute the perovskite can move when an external electric field is applied. A switching of photocurrent in the device depending on bias was shown by *Huang et al.*[70] and was explained by ion-migration. A perovskite layer was sandwiched between p-type materials in their research. So, they concluded that depending on the direction of the applied bias, ions are either migrating towards the bulk or are accumulating towards the interface. This in turn causes the electric field inside the

material to change, due to which the device used in their work was showing switching photovoltaic behavior.[72] Since their work, it has been shown that there is also a chemical and morphological change in the device when an electric field is applied. In their work, the device underwent conversion of hybrid perovskite MAPI to  $\text{PbI}_2$  and MAI when an electric field as low as  $3 \text{ V } \mu\text{m}^{-1}$  was applied. This interconversion was explained by the ions diffusing within the perovskite layer at temperatures greater than 300K. This mechanism is shown in Figure 35. This was the first visual proof of ion-migration in perovskite which is reversible and can be caused by electric poling. [66]By referencing these studies, it can be said that the positively charged cations and negatively charged anions are spread out uniformly in the bulk perovskite. But, due to the effect of an electric field, the cations and anions move towards perovskite-HTL interface and perovskite-ETL interface respectively during normal operation. This process changes the J-V characteristic of the solar cell. Hence, the change in capacitance can be linked to the mobile ions that are migrating from the MAPI towards the HTL.

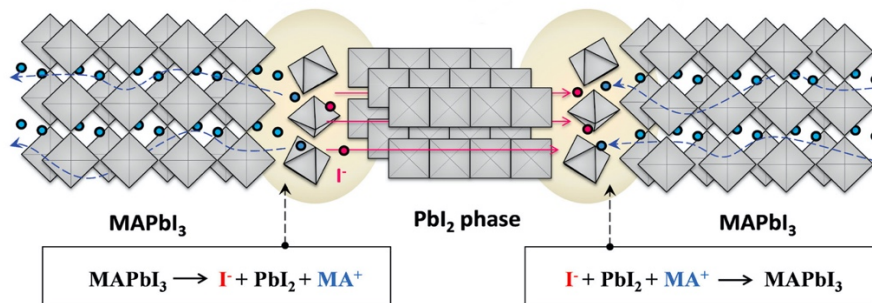


**Figure 35: Interconversion of MAPI due to ion migration [65]**

Now that ion-migration has been linked to the change in capacitance in the device

fabricated in this work, another question remains about what species is migrating.

Various results have been reported regarding the activation energy of ion migration in MAPI due to associated ions. The reported activation energies,  $E_a$ , range as low as 0.1 eV to 0.58 eV and has been reported to be connected to mobile I<sup>-</sup> ions. Furthermore, the activation energy associated with MA cations and Iodine anions is low compared to that of Pb<sup>2+</sup>[73] [74][75][72][76][77]. For the devices used to measure the transient capacitance for various temperatures, the activation energy was found to be 220meV which is close to the values reported in the literature. The Arrhenius plot for decay rate of fast exponential component using two exponential fit of capacitance decay is shown in Figure 36.

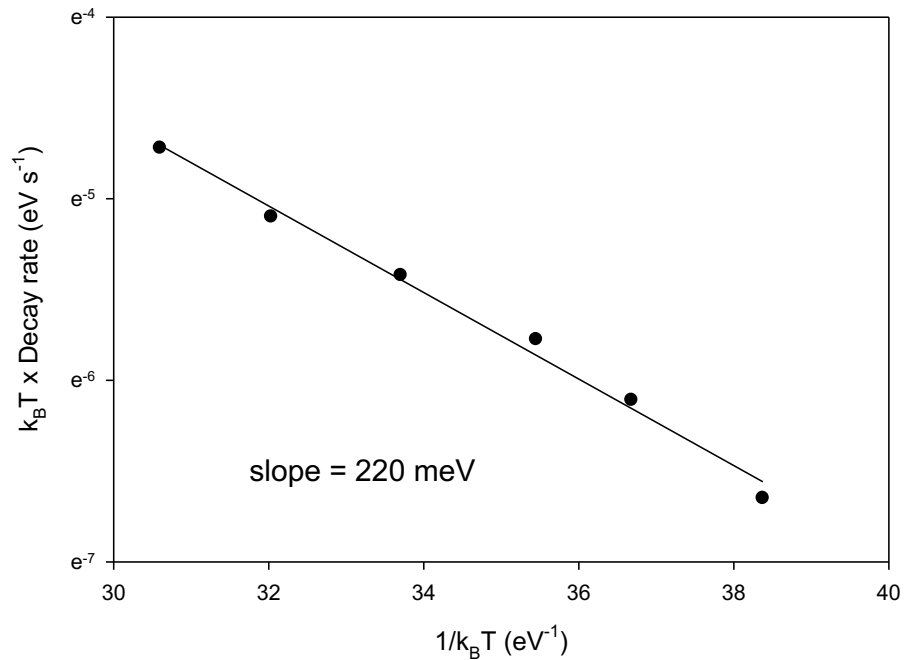


**Figure 36: Arrhenius plot of the decay rate of the fast exponential component in a two exponential fit of capacitance decay for solar cell with PTAA HTL**

The rate of ion migration is inversely proportional to the exponential of the

activation energy and can be written as:

$$r = \exp\left(-\frac{E_A}{k_B T}\right) \quad (10)$$

where,  $r$ , is the rate of capacitance decay,  $k_B$  is the Boltzmann constant and  $T$  is the temperature. The above graph was plotted with the help of this equation which can be simplified to fit a double exponential whose slope will be the activation energy. Now that the mechanism for the recovery of perovskite solar cells has been explored, this work will now try to identify the migrating species in the devices used for this work.

### 3.7 Energy dispersive X-Ray spectroscopy

Energy dispersive X-Ray spectroscopy (EDX) is a technique which can detect the element present in the sample. It is a widely used technique which is used jointly with the scanning electron microscope (SEM). This method can be utilized to gather information about the chemical composition in a material of interest.

EDX will be used to further investigate if any chemical change has occurred in the sample after light soaking and electric poling. However, there were no changes visually to the device that underwent electrical poling. So, this technique will be used to further investigate if any iodine ions have migrated towards the HTL. To facilitate the experiment, the device encapsulation was removed, and the device was dipped in DMF solution to remove the perovskite layer. The device was dissolved in DMF three times in separate beakers to avoid having the residue of perovskite on the resulting sample. This process resulted in glass/ITO/PTAA/C<sub>60</sub>/BCP/Al structure which is shown in Figure 37.

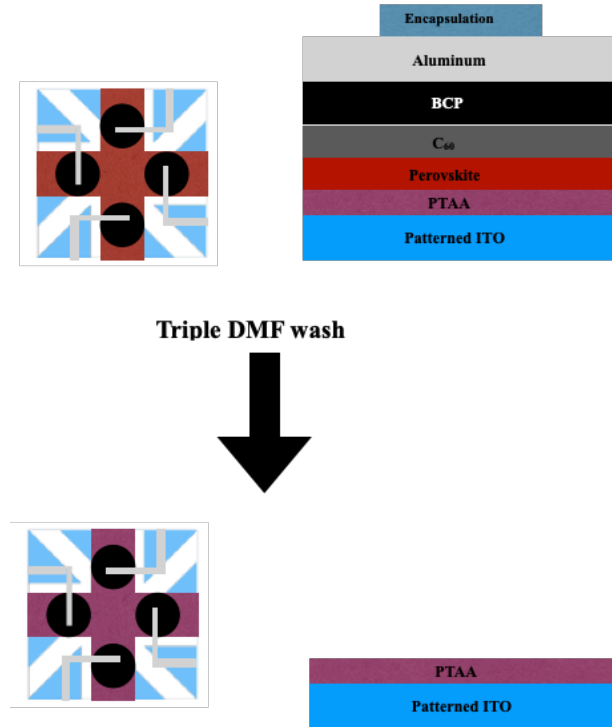


**Figure 37: Removal of Perovskite layer with triple DMF wash**

To compare if any chemical changes occurred after electrical biasing, a full device prior to DMF washing and a device after biasing was tested with EDX. After performing J-V acquisition, the sample was kept inside the glovebox, with  $\sim 0$  ppm O<sub>2</sub> and moisture, for two days enclosed in a sample holder which was wrapped in aluminum foil to prevent light exposure. Then, the sample was biased with +1V with Keithly 2400 SourceMeter for 10 minutes. Following this, the sample was taken out of the glovebox and washed with DMF. Besides performing EDX on the device that had been inside the glovebox for 2 days, a fresh device was also tested. The EDX spectra for the fresh device and device without perovskite are shown respectively in Figures 38 and 39.

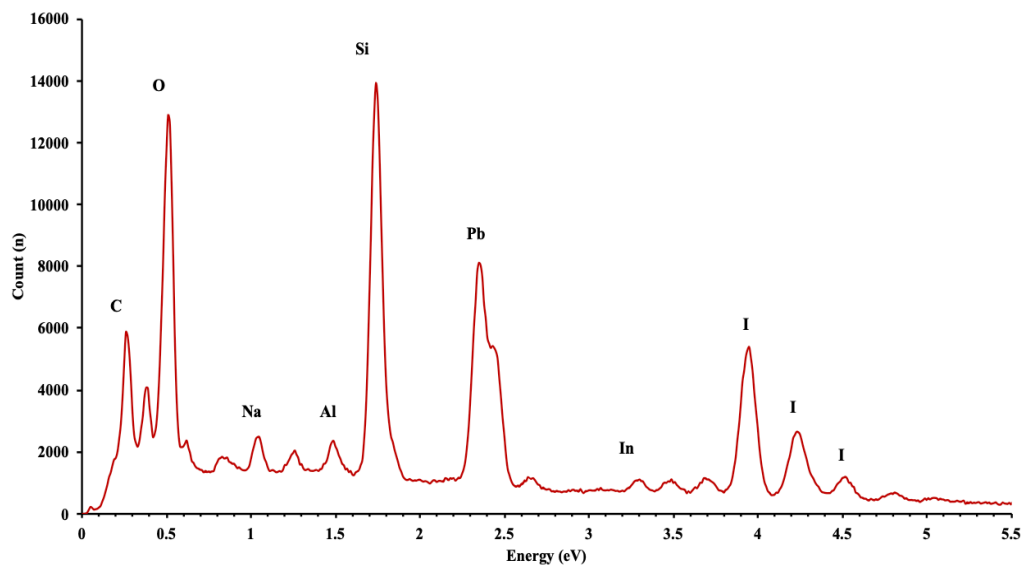


**Figure 38: EDX result of fresh device with PTAA HTL**

The results for fresh device showed that it has substantial amount of Carbon(C), Oxygen (O), Sodium (Na), Aluminum (Al), Silicon (Si), Lead (Pb), Indium (In) and Iodine (I). These detection of these elements can be correlated to the presence of contact layer: Al and In , glass: O, Na, Si [78] and the perovskite layer Pb, I and C. The presence of these elements suggest that the device has all the layers present.

The device which was biased did not have any peaks for Pb and Iodine, which confirmed that the perovskite was removed. However, this reasoning might be due to the peaks of Indium and Iodine having the excitation around same energy level.[79] Further fitting of the EDX peaks could not confirm the presence of Iodine peak at 3.937 eV. Moreover, the count of Iodine ions migrating towards the HTL could also be one of the reasons for the measurement having no counts for Iodine peaks. Further experimental methodology which is beyond the current availability at Texas State University is required to confirm the presence of Iodine ion.

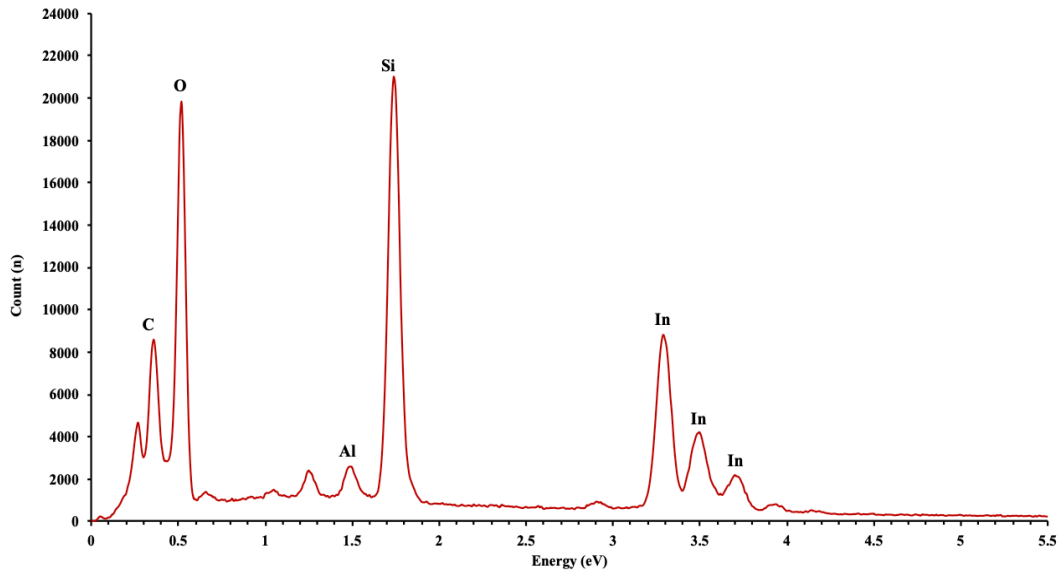


**Figure 39: EDX results of device without perovskite**

Finally, it is of great importance to further understand how mobile ions are migrating due to electric field because this could offer gateways to further stabilize perovskite solar cells. As mentioned earlier, hybrid perovskites have a crystal structure which certainly have defects due to which it is believed to form ion migration channels. There have been theoretical calculations to show that these channels are formed through point defects, surface and grain boundaries, lattice distortion and strains due to piezoelectric effect. Among these, activation energy for migration through grain boundaries is almost half among other mechanisms. [80] These are shown in Figure 40.

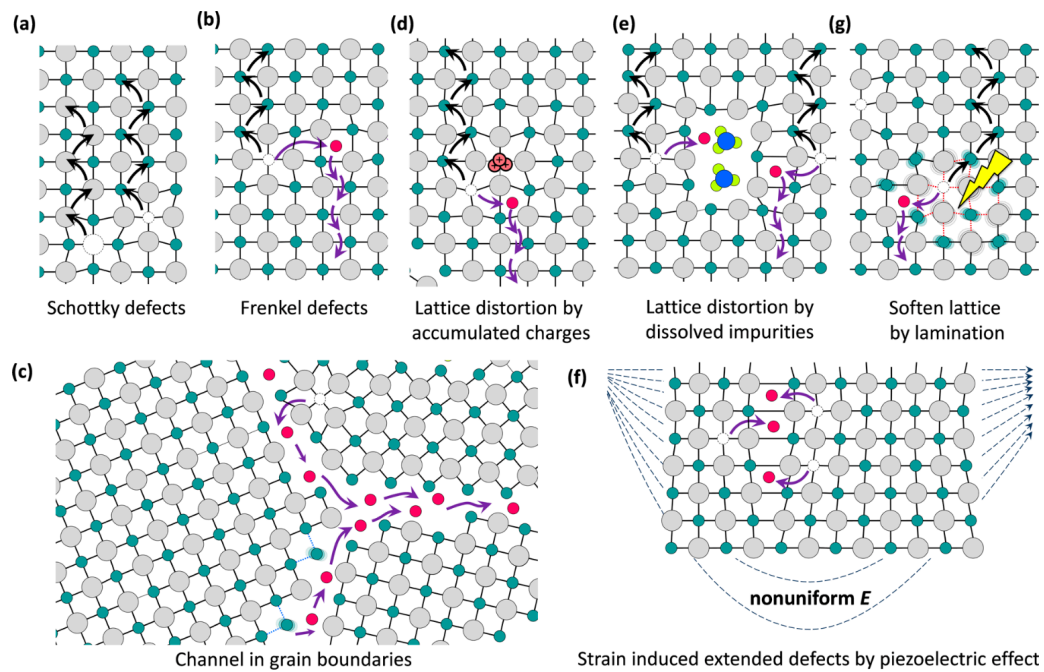


**Figure 40: Ion migration channels in hybrid halide perovskites [80]**

#### 4. CONCLUSIONS

In this work, firstly PTAA thin films of different thickness were investigated as a potential HTL in perovskite solar cell of inverted planar heterojunction structure with glass/ITO/PTAA/MAPI/C<sub>60</sub>/BCP/Al architecture. PTAA powder of different weights were dissolved in toluene to have PTAA solutions of different concentrations which required low thermal processing in order to deposit PTAA thin film on ITO. The process parameters involved to deposit the HTL were sensibly improved by varying the concentration of the precursor and RPMs of the spin coater to deposit the HTL. The optimization process concluded when the highest quality HTLs were produced to achieve comparatively superior performance among the sample population. After achieving this goal, the HTL samples were characterized to determine the thickness, morphology and the bandgap of the HTL.

The unoptimized PTAA thin films had a random and rough sponge like texture which was revealed by AFM images. The profilometry measurements used to determine the thickness of the HTL to be  $8.5\pm 0.8$  nm,  $15.4\pm 0.7$  nm and  $24.8\pm 0.9$  nm for 2mg/ml, 3mg/ml and 4mg/ml respectively. These HTLs were deposited using optimized RPMs for spin coating. PTAA HTL of 2mg/ml had a roughness of 2.13nm which was measured using AFM. This was the highest number for RMS roughness among the PTAA samples.

UV-Vis measurement was used to understand the optical transmission and absorbance for the HTL using glass/ITO as reference. The results indicated that the HTL had excellent optical transmission of about 90% in the wavelength range of 425nm to 900nm. The wrinkles in the transmission graph at 384nm was characteristic to that of PTAA HTL which was confirmed with other works. Absorbance data from UV-Vis was

used to estimate the band gap of the material, which was approximately 3.22 eV. This value is close to expected values for band gap of PTAA from available literature.

Upon optimizing the process parameters and performing some preliminary characterization of PTAA HTL, the HTL was incorporated into the device architecture of perovskite PV cell glass/ITO/HTL/MAPI/C<sub>60</sub>/BCP/Al. The different concentrations of PTAA HTL were used to fabricate devices whose average PCE ranged from 13.40±1.19% to 16.64±0.77%. The lowest average PCE was from the samples having 4mg/ml PTAA in toluene and the highest was recorded from samples with 2mg/ml PTAA in toluene. The champion device with PTAA HTL had an average PCE of 17.7% with a V<sub>OC</sub> of 1.04 V, FF of 79.61% and a J<sub>SC</sub> of -21.38mA/cm<sup>2</sup>. Devices with 2mg/ml PTAA concentration consistently had higher performance metrics compared to devices which utilized other concentration of PTAA. The EQE result for the solar cell with the optimized process parameter for the HTL was around 80% which means that a reasonable amount of the photons incident on the solar cell is being converted to electrons in the range of 400nm to 650nm which is within the visible range. This fact also elucidated that the device performs reasonably well in the visible range.

After the electrical characterization, the J-V curves obtained for all the samples utilized in this work were fitted with a two-diode model to calculate the values for series resistance  $R_S$ , shunt resistance  $R_P$  and the ideality factor through the second diode  $n_2$ . The ideality factor through the first diode was fixed as 1 as there are two possible mechanism of recombination that could be happening in the solar cell, and an ideality factor of 1 represents band-to-band recombination during low injection of carriers. As the method of fitting an equation with parameters for two diode required complex numerical method

which could be tedious and require complex calculations, a MATLAB standalone executable program was used in order to facilitate the calculation of the parameters. The champion device with PTAA HTL had an ideality factor of 2.2 with a  $R_S$  of  $3.09\Omega\cdot\text{cm}^2$  and  $R_P$  of  $5.07\text{k}\Omega\cdot\text{cm}^2$ . Moreover, the currents through the two diodes,  $J_{01}$  and  $J_{02}$ , were calculated as  $5.36\cdot 10^{-17}$  mA/cm<sup>2</sup> and  $7.65\cdot 10^{-8}$  mA/cm<sup>2</sup> respectively.

A temperature and illumination dependent study of the device with optimized process parameters was done to investigate stability. It was found that upon changing the illumination intensity, the short circuit current of the device changes logarithmically and the open circuit voltage had a linear change. Moreover, upon conducting an investigation of temperature-based J-V characteristic in the regime of 134K to 374K, it was found that the  $V_{OC}$  varied between 0.82 V (T = 134 K) to 1.02 V (T = 290 K). This could be attributed to the phase change of the hybrid halide perovskite absorber layer  $\text{CH}_3\text{NH}_3\text{PbI}_3$  from orthorhombic (T < 165K) to tetragonal (T = 165 K to 327 K) to cubic (T > 327 K).

A light soaking and bias dependent study for the devices was carried out to study the stability of the devices. It was found that the devices degraded in performance when left in dark for a few hours. However, the process of degradation was reversible and could be changed either with light soaking or with applying bias. Upon light soaking, the performance of the devices was restored but there was a loss in short circuit current, which we hypothesize to be because of heating. The biasing in PTAA based HTL devices led to the recovery in performance which was caused due to ion migration of iodine ions in the perovskite absorber layer. To prove this, the activation energy was calculated using an Arrhenius plot with a magnitude of 220meV. This activation energy calculated in this work was close to that of the values found in literature for iodine ions.

For further verification of ion-migration, EDX measurement was carried out by washing the device with DMF. However, no noticeable trace of iodine was detected which could be due to the count of iodine ions that migrate towards the HTL. Experimental capabilities beyond the scope of this research will be required to appropriately detect the amount of iodine ions. This is left as a recommendation for future work for the devices with PTAA HTL.

### **Considerations for Future Work**

It must be noted that there are some items that lacked exposure in this research that could be a recommendation for future work regarding the devices investigated here. As PTAA and ITO are both transparent in visible range, it is quite challenging to accurately model the ITO/PTAA stack using spectroscopic ellipsometry. Due to this, PTAA could be spin coated on Silicon wafer to reduce the backside reflection and correctly obtain ellipsometry data. There are some derivatives of PTAA polymer that could be compared to pristine PTAA by employing the same experimental techniques. Also, the ion-migration is in perovskite layer, the layer could be further explored by either mixing it with other halides or adding ligands which have shown to passivate ion migration and increase device stability and performance.[81] Other experimental techniques such as X-Ray photon spectroscopy and Tunneling Electron Microscopy could be used to investigate and verify temperature dependent chemical change of the solar cells. Further optimization could be done for ETL by varying the thickness of it or employing other known ETLs such as PCBM or Zinc Oxide (ZnO). Similar studies could be carried out employing these layers to further study the stability of the devices.

## **APPENDIX SECTION**

The purpose of this section is to provide supplementary information about equipment and measurement specification for the characterization methods used in this research. The materials enlisted is given in order to reproduce the reported methodology and results.

### **Surface Profilometer**

The stylus profilometer used was the Bruker Dektak XT. The radius of the stylus was 2  $\mu\text{m}$  with a stylus tip force of 3 mg. All the scans had a length of 500 nm.

### **Atomic Force Microscopy**

The AFM equipment model was the Bruker Dimension ICON. All the measurement were taken in “tapping mode” in normal atmosphere. The tip type HQ:NSC14/AL BS was used in the AFM which has an average operating frequency of 160 kHz with an average force constant of 5 N/m.

### **Ultraviolet-Visible Spectroscopy**

A Shimadzu UV-2501PC was used to obtain UV-Vis data which supports Transmittance, absorbance and reflectance modes. The wavelength range permitted by the tool was 190 to 1100nm with a resolution of 0.1 nm. Sample measurement for this work was done in the range of 200- 900 nm.

### **Energy Dispersive X-Ray Spectroscopy**

The SEM equipment FEI Helios NanoLab 4000 was used to acquire EDX

measurements. The acceleration voltage and beam current were kept the same during SEM focusing and EDX measurements. The scan voltage of 10 kV and a beam current 0.34 nA was used for both sample type.

### **Device J-V Characterization**

The photovoltaic device produced for this work were characterized with a ORIEL solar simulator under AM 1.5G illumination. The J-V curves were acquired using a Keithley 2400 SourceMeter multimeter. A LabView program especially coded for this characterization was used to collect the data. The program calculated all the performance metric such as: FF,  $J_{SC}$ ,  $V_{OC}$ , PCE.

### **ARS Cryoprobe Station**

Temperature and Illumination dependent J-V curve were acquired using Advanced Research System probe station. The temperature was varied using LakeShore 336 temperature controller with He compressor in the intervals of 20K. The current-voltage measurement was acquired using a KEYSIGHT B2912A source meter. The light intensity of the Energetiq LDLS light source was varied using Optical density filters.

### **Two-Diode Modeling**

The standalone executable file was downloaded from the reference mentioned in two-diode section. The program allowed to input temperature and area of the device which for this work was 24°C and 0.0625 cm<sup>2</sup> respectively. The user interface of the program is shown in Figure 41. The checkmarks on the left represent what parameters are

allowed to float. To fit the data into this model ,first, single diode parameters ( $J_{01}$ ,  $R_{par}, R_{ser}, n_1$ ) was allowed to float. Then, the obtained parameters were used to float all the parameters ( $J_{01}, n_1, J_{01}, n_2, R_{par}, R_{ser}$ ) where  $n_1$  and  $n_2$  were guessed as 1 and 2 respectively.

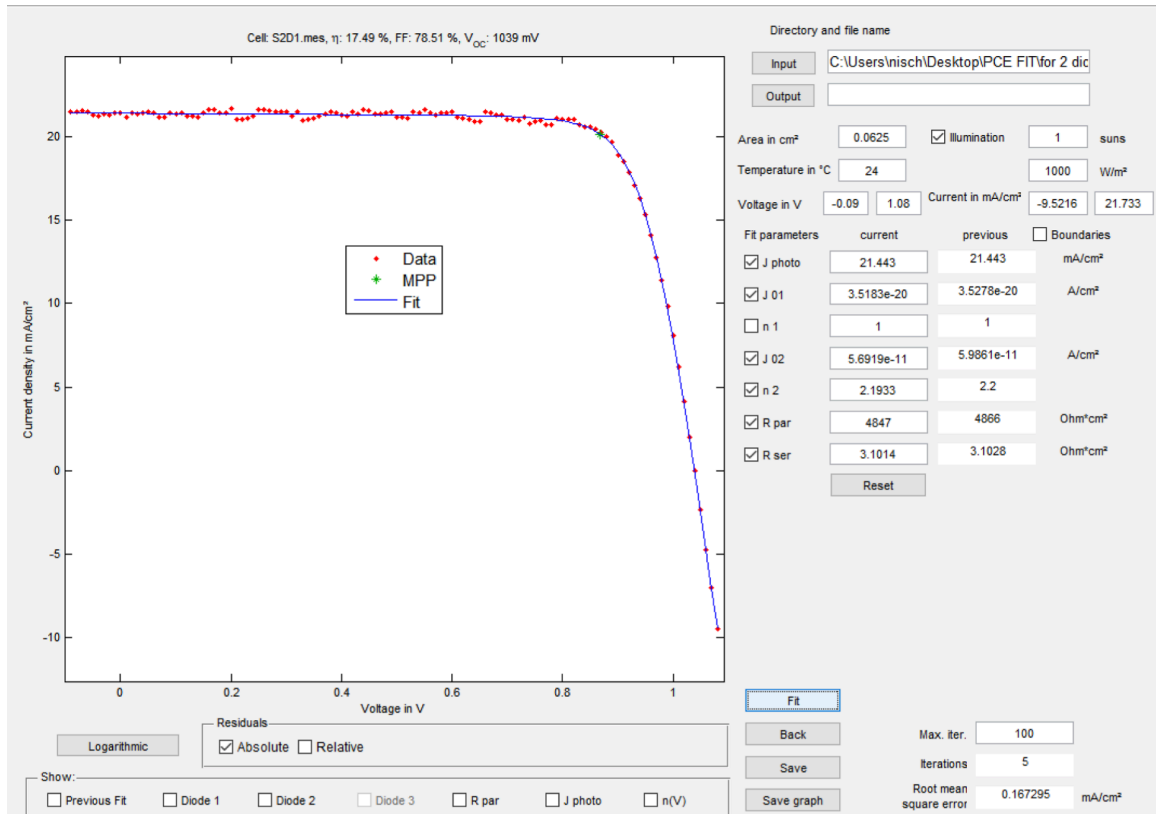


**Figure 41: Standalone executable program for 2-diode fit**

## REFERENCES

- [1] Edmond Becquerel, "Comptes rendus hebdomadaires des séances de l' Académie des sciences / publiés ... par MM . les secrétaires," *Comptes rendus*, vol. 9, pp. 561–567, 1839.
- [2] P. John, "6000 Years of Solar Architecture and Technology." 2013.
- [3] "This Month in Physics History." 2009.
- [4] NREL, "Best Research-Cell Efficiencies: Rev. 04-06-2020." 2020.
- [5] A. Navrotsky, "Energetics and Crystal Chemical Systematics among Ilmenite, Lithium Niobate, and Perovskite Structures," *Chem. Mater.*, vol. 10, no. 10, pp. 2787–2793, Oct. 1998.
- [6] T.-B. Song *et al.*, "Under the spotlight: The organic–inorganic hybrid halide perovskite for optoelectronic applications," *Nano Today*, vol. 10, no. 3, pp. 355–396, 2015.
- [7] D. Weber, "CH<sub>3</sub>NH<sub>3</sub>PbX<sub>3</sub>, ein Pb(II)-System mit kubischer Perowskitstruktur," *Z. Naturforsch., B J. Chem. Sci.*, vol. 1445, no. August, pp. 1443–1445, 1978.
- [8] D. B. Mitzi, "Synthesis, Structure, and Properties of Organic-Inorganic Perovskites and Related Materials," *Progress in Inorganic Chemistry*. pp. 1–121, 01-Jan-1999.
- [9] K. A. T. K, S. Y, and M. T, "Organometal halide perovskites as visible-light sensitizers for photovoltaic cells," *J. Am. Chem. Soc.*, vol. 131, no. 17, pp. 6050–1, 2009.

- [10] J.-H. Im, C.-R. Lee, J.-W. Lee, S.-W. Park, and N.-G. Park, “6.5% efficient perovskite quantum-dot-sensitized solar cell,” *Nanoscale*, vol. 3, no. 10, pp. 4088–4093, 2011.
- [11] A. K. Jena, A. Kulkarni, and T. Miyasaka, “Halide Perovskite Photovoltaics: Background, Status, and Future Prospects,” *Chem. Rev.*, vol. 119, no. 5, pp. 3036–3103, Mar. 2019.
- [12] M. M. Lee, J. Teuscher, T. Miyasaka, T. N. Murakami, and H. J. Snaith, “Efficient Hybrid Solar Cells Based on Meso-Superstructured Organometal Halide Perovskites,” *Science (80-. )*, vol. 338, no. 6107, pp. 643 LP – 647, Nov. 2012.
- [13] J. H. Noh, S. H. Im, J. H. Heo, T. N. Mandal, and S. Il Seok, “Chemical Management for Colorful, Efficient, and Stable Inorganic–Organic Hybrid Nanostructured Solar Cells,” *Nano Lett.*, vol. 13, no. 4, pp. 1764–1769, Apr. 2013.
- [14] C. C. Stoumpos, C. D. Malliakas, and M. G. Kanatzidis, “Semiconducting Tin and Lead Iodide Perovskites with Organic Cations: Phase Transitions, High Mobilities, and Near-Infrared Photoluminescent Properties,” *Inorg. Chem.*, vol. 52, no. 15, pp. 9019–9038, Aug. 2013.
- [15] S. Rühle, “Tabulated values of the Shockley–Queisser limit for single junction solar cells,” *Sol. Energy*, vol. 130, pp. 139–147, 2016.
- [16] W. W. Yin, J. J. Yang, J. Kang, Y. Yan, and S. Wei, “Halide Perovskite Materials for Solar Cells: A Theoretical Review,” *J. Mater. Chem. A*, vol. 3, no. 17, pp. 8926–8942, 2015.

- [17] P. Tonui, S. O. Oseni, G. Sharma, Q. Yan, and G. Tessema Mola, “Perovskites photovoltaic solar cells: An overview of current status,” *Renew. Sustain. Energy Rev.*, vol. 91, no. November 2017, pp. 1025–1044, 2018.
- [18] C. Manspecker, S. Venkatesan, A. Zakhidov, and K. S. Martirosyan, “Role of interface in stability of perovskite solar cells,” *Current Opinion in Chemical Engineering*, vol. 15. Elsevier Ltd, pp. 1–7, 01-Feb-2017.
- [19] A. Fakharuddin, L. Schmidt-Mende, G. Garcia-Belmonte, R. Jose, and I. Mora-Sero, “Interfaces in Perovskite Solar Cells,” *Adv. Energy Mater.*, vol. 7, no. 22, p. 1700623, Nov. 2017.
- [20] F. Meillaud, A. Shah, C. Droz, E. Vallat-Sauvain, and C. Miazza, “Efficiency limits for single-junction and tandem solar cells,” *Sol. Energy Mater. Sol. Cells*, vol. 90, no. 18, pp. 2952–2959, 2006.
- [21] A. L. Abdelhady *et al.*, “Heterovalent Dopant Incorporation for Bandgap and Type Engineering of Perovskite Crystals,” *J. Phys. Chem. Lett.*, vol. 7, no. 2, pp. 295–301, Jan. 2016.
- [22] J.-Y. Seo *et al.*, “Novel p-dopant toward highly efficient and stable perovskite solar cells,” *Energy Environ. Sci.*, vol. 11, no. 10, pp. 2985–2992, 2018.
- [23] “Solar Cell Structure | PVEducation.” 03-Jun-2020.
- [24] X. Chen, H. Lu, Y. Yang, and M. C. Beard, “Excitonic Effects in Methylammonium Lead Halide Perovskites,” *J. Phys. Chem. Lett.*, vol. 9, no. 10, pp. 2595–2603, 2018.
- [25] N. Bohr, “I. On the constitution of atoms and molecules,” *London, Edinburgh, Dublin Philos. Mag. J. Sci.*, vol. 26, no. 151, pp. 1–25, Jul. 1913.

- [26] T. S. Sherkar *et al.*, “Recombination in Perovskite Solar Cells: Significance of Grain Boundaries, Interface Traps, and Defect Ions,” *ACS Energy Lett.*, vol. 2, no. 5, pp. 1214–1222, 2017.
- [27] G. J. A. H. Wetzelaer, M. Scheepers, A. M. Sempere, C. Momblona, J. Ávila, and H. J. Bolink, “Trap-Assisted Non-Radiative Recombination in Organic-Inorganic Perovskite Solar Cells,” *Adv. Mater.*, vol. 27, no. 11, pp. 1837–1841, 2015.
- [28] D. Emin, “Barrier to recombination of oppositely charged large polarons,” *J. Appl. Phys.*, vol. 123, no. 5, 2018.
- [29] F. Zheng, L. Z. Tan, S. Liu, and A. M. Rappe, “Rashba spin-orbit coupling enhanced carrier lifetime in CH<sub>3</sub>NH<sub>3</sub>PbI<sub>3</sub>,” *Nano Lett.*, vol. 15, no. 12, pp. 7794–7800, 2015.
- [30] L. M. Pazos-Outón *et al.*, “Photon recycling in lead iodide perovskite solar cells,” *Science (80-. )*, vol. 351, no. 6280, pp. 1430 LP – 1433, Mar. 2016.
- [31] J. M. Frost, K. T. Butler, F. Brivio, C. H. Hendon, M. van Schilfgaarde, and A. Walsh, “Atomistic origins of high-performance in hybrid halide perovskite solar cells,” *Nano Lett.*, vol. 14, no. 5, pp. 2584–2590, 2014.
- [32] Y. Shao *et al.*, “Grain boundary dominated ion migration in polycrystalline organic–inorganic halide perovskite films,” *Energy Environ. Sci.*, vol. 9, no. 5, pp. 1752–1759, 2016.
- [33] P. Cui *et al.*, “Reduced surface defects of organometallic perovskite by thermal annealing for highly efficient perovskite solar cells,” *RSC Adv.*, vol. 5, no. 92, pp. 75622–75629, 2015.

- [34] X. Wu *et al.*, “Trap States in Lead Iodide Perovskites,” *J. Am. Chem. Soc.*, vol. 137, no. 5, pp. 2089–2096, Feb. 2015.
- [35] W.-J. Yin, T. Shi, and Y. Yan, “Unusual defect physics in CH<sub>3</sub>NH<sub>3</sub>PbI<sub>3</sub> perovskite solar cell absorber,” *Appl. Phys. Lett.*, vol. 104, no. 6, p. 063903, 2014.
- [36] A. J. Neukirch *et al.*, “Polaron stabilization by cooperative lattice distortion and cation rotations in hybrid perovskite materials,” *Nano Lett.*, vol. 16, no. 6, pp. 3809–3816, May 2016.
- [37] W. Nie *et al.*, “Light-activated photocurrent degradation and self-healing in perovskite solar cells,” *Nat. Commun.*, vol. 7, no. May, pp. 1–9, 2016.
- [38] “2.11 Carrier generation and recombination.” 03-Jun-2020.
- [39] R. L. Milot, G. E. Eperon, H. J. Snaith, M. B. Johnston, and L. M. Herz, “Temperature-Dependent Charge-Carrier Dynamics in CH<sub>3</sub>NH<sub>3</sub>PbI<sub>3</sub> Perovskite Thin Films,” *Adv. Funct. Mater.*, vol. 25, no. 39, pp. 6218–6227, Oct. 2015.
- [40] P. Calado *et al.*, “Identifying Dominant Recombination Mechanisms in Perovskite Solar Cells by Measuring the Transient Ideality Factor,” *Phys. Rev. Appl.*, vol. 11, no. 4, p. 44005, Apr. 2019.
- [41] K. Lyon, “Copper iodide and copper (i) oxide based hole transport materials for methylammonium lead iodide photovoltaic device optimization.” 2019.
- [42] S. Suckow, T. M. Pletzer, and H. Kurz, “Fast and reliable calculation of the two-diode model without simplifications,” *Prog. Photovoltaics Res. Appl.*, vol. 22, no. 4, pp. 494–501, 2014.
- [43] “Physics of Solar Cells.” 03-Jun-2020.

- [44] A. H. M. Smets, K. Jäger, O. Isabella, R. A. van Swaaij, and M. Zeman, “Solar Cell Parameters and Equivalent Circuit 9.1 External solar cell parameters,” *Sol. energy Phys. Eng. Photovolt. conversion, Technol. Syst.*, pp. 113–121, 2016.
- [45] C. C. Gonzalez and R. G. Ross, “Performance measurement reference conditions for terrestrial photovoltaics,” 1980.
- [46] W. Shockley and H. J. Queisser, “Detailed balance limit of efficiency of p-n junction solar cells,” *J. Appl. Phys.*, vol. 32, no. 3, pp. 510–519, 1961.
- [47] N.-G. Park and H. Segawa, “Research Direction toward Theoretical Efficiency in Perovskite Solar Cells,” *ACS Photonics*, vol. 5, no. 8, pp. 2970–2977, Aug. 2018.
- [48] “Spin Coating: Complete Guide to Theory and Techniques,” *Ossila*. 03-Jul-2020.
- [49] S. Venkatesan *et al.*, “Tailoring nucleation and grain growth by changing the precursor phase ratio for efficient organic lead halide perovskite optoelectronic devices,” *J. Mater. Chem. C*, vol. 5, no. 39, pp. 10114–10121, 2017.
- [50] C. Chen *et al.*, “Effect of BCP buffer layer on eliminating charge accumulation for high performance of inverted perovskite solar cells,” *RSC Adv.*, vol. 7, no. 57, pp. 35819–35826, 2017.
- [51] “Atomic force microscopy,” *Wikipedia*. 03-Jun-2020.
- [52] H.-H. Perkampus, *UV-VIS Spectroscopy and Its Applications*. Berlin, Heidelberg: Springer Berlin Heidelberg, 1992.
- [53] “Analytical chemistry - UV visible spectroscopy.” 03-Jun-2020.
- [54] A. McEvoy, L. Castaner, T. Markvart, and an O. M. C. Safari, *Solar Cells, 2nd Edition*. 2012.

- [55] T. J. K. Brenner, Y. Vaynzof, Z. Li, D. Kabra, R. H. Friend, and C. R. McNeill, “White-light bias external quantum efficiency measurements of standard and inverted P3HT:PCBM photovoltaic cells,” *J. Phys. D. Appl. Phys.*, vol. 45, no. 41, 2012.
- [56] J. Endres *et al.*, “Electronic structure of the CsPbBr<sub>3</sub>/polytriarylamine (PTAA) system,” *J. Appl. Phys.*, vol. 121, no. 3, 2017.
- [57] P. Calado *et al.*, “Identifying Dominant Recombination Mechanisms in Perovskite Solar Cells by Measuring the Transient Ideality Factor,” *Phys. Rev. Appl.*, vol. 11, no. 4, p. 1, 2019.
- [58] N. Enebish, D. Agchbayar, S. Dorjkhand, D. Baatar, and I. Ylemj, “Numerical analysis of solar cell current-voltage characteristics,” *Sol. Energy Mater. Sol. Cells*, vol. 29, no. 3, pp. 201–208, 1993.
- [59] B. V Van Zeghbroeck, *Principles of semiconductor devices and heterojunctions*. Upper Saddle River, N.J.; London: Prentice Hall ; Pearson Education [distributor, 2010.
- [60] L. Contreras-Bernal *et al.*, “Homeopathic Perovskite Solar Cells: Effect of Humidity during Fabrication on the Performance and Stability of the Device,” *J. Phys. Chem. C*, vol. 122, no. 10, pp. 5341–5348, Mar. 2018.
- [61] S. W. Lee *et al.*, “UV Degradation and Recovery of Perovskite Solar Cells,” *Sci. Rep.*, vol. 6, pp. 1–10, 2016.
- [62] T. A. Berhe *et al.*, “Organometal halide perovskite solar cells: degradation and stability,” *Energy Environ. Sci.*, vol. 9, no. 2, pp. 323–356, 2016.

- [63] G. Divitini, S. Cacovich, F. Matteocci, L. Cinà, A. Di Carlo, and C. Ducati, “In situ observation of heat-induced degradation of perovskite solar cells,” *Nat. Energy*, vol. 1, no. 2, p. 15012, 2016.
- [64] M. Wang, W. L. Yim, P. Liao, and Y. Shen, “Temperature Dependent Characteristics of Perovskite Solar Cells,” *ChemistrySelect*, vol. 2, no. 16, pp. 4469–4477, 2017.
- [65] Z. Xiao *et al.*, “Giant switchable photovoltaic effect in organometal trihalide perovskite devices,” *Nat. Mater.*, vol. 14, no. 2, pp. 193–197, 2015.
- [66] Y. Yuan *et al.*, “Electric-field-driven reversible conversion between methylammonium lead triiodide perovskites and lead iodide at elevated temperatures,” *Adv. Energy Mater.*, vol. 6, no. 2, pp. 1–7, 2016.
- [67] E. L. Unger *et al.*, “Hysteresis and transient behavior in current-voltage measurements of hybrid-perovskite absorber solar cells,” *Energy Environ. Sci.*, vol. 7, no. 11, pp. 3690–3698, 2014.
- [68] A. Zamouche, T. Heiser, and A. Mesli, “Investigation of fast diffusing impurities in silicon by a transient ion drift method,” *Appl. Phys. Lett.*, vol. 631, no. November 1994, p. 631, 1995.
- [69] I. Lyubomirsky, M. K. Rabinal, and D. Cahen, “Room-temperature detection of mobile impurities in compound semiconductors by transient ion drift,” *J. Appl. Phys.*, vol. 81, no. 10, pp. 6684–6691, 1997.
- [70] M. H. Futscher *et al.*, “Quantification of ion migration in CH<sub>3</sub>NH<sub>3</sub>PbI<sub>3</sub> perovskite solar cells by transient capacitance measurements,” *Mater. Horizons*, vol. 6, no. 7, pp. 1497–1503, Aug. 2019.

- [71] T. Heiser and A. Mesli, “from Transient Ion-Drift,” *Physics (College. Park. Md).*, vol. 328, pp. 325–328, 1993.
- [72] Y. Yuan *et al.*, “Photovoltaic Switching Mechanism in Lateral Structure Hybrid Perovskite Solar Cells,” *Adv. Energy Mater.*, vol. 5, no. 15, pp. 1–7, 2015.
- [73] C. Eames, J. M. Frost, P. R. F. Barnes, B. C. O’Regan, A. Walsh, and M. S. Islam, “Ionic transport in hybrid lead iodide perovskite solar cells,” *Nat. Commun.*, vol. 6, p. 7497, Jun. 2015.
- [74] O. Almora, I. Zarazua, E. Mas-Marza, I. Mora-Sero, J. Bisquert, and G. Garcia-Belmonte, “Capacitive dark currents, hysteresis, and electrode polarization in lead halide perovskite solar cells,” *J. Phys. Chem. Lett.*, vol. 6, no. 9, pp. 1645–1652, 2015.
- [75] T.-Y. Yang, G. Gregori, N. Pellet, M. Grätzel, and J. Maier, “The Significance of Ion Conduction in a Hybrid Organic-Inorganic Lead-Iodide-Based Perovskite Photosensitizer,” *Angew. Chemie*, vol. 127, no. 27, pp. 8016–8021, 2015.
- [76] J. Haruyama, K. Sodeyama, L. Han, and Y. Tateyama, “First-principles study of ion diffusion in perovskite solar cell sensitizers,” *J. Am. Chem. Soc.*, vol. 137, no. 32, pp. 10048–10051, 2015.
- [77] J. M. Azpiroz, E. Mosconi, J. Bisquert, and F. De Angelis, “Defect migration in methylammonium lead iodide and its role in perovskite solar cell operation,” *Energy Environ. Sci.*, vol. 8, no. 7, pp. 2118–2127, 2015.
- [78] S. Ghosh, N. Dandapat, and V. K. Balla, “Preparation and in vitro Characterization of Fluoroapatite Based Bioactive Glass-ceramics for Biomedical Applications,” *Mater. Today Proc.*, vol. 2, no. 4–5, pp. 1326–1331, 2015.

- [79] EDS\_Ref, “X-Ray Energies of the Elements,” *Eds*, pp. 0–1.
- [80] Y. Yuan and J. Huang, “Ion Migration in Organometal Trihalide Perovskite and Its Impact on Photovoltaic Efficiency and Stability,” *Acc. Chem. Res.*, vol. 49, no. 2, pp. 286–293, 2016.
- [81] X. Zheng *et al.*, “Managing grains and interfaces via ligand anchoring enables 22.3%-efficiency inverted perovskite solar cells,” *Nat. Energy*, 2020.